Moderate solvation structure of lithium ions for high-voltage lithium metal batteries at –40ºC

Ying Wei,[a] Han Wang,[b] Xing Lin,[a] Tianyu Wang,[b] Yanming Cui,[c] Yu Huang,[a] Jiayi Yang,[d] Te-Huan Liu,*[b] Yang Ren,[d] Xiulin Fan,[e] Henghui Xu*[a] and Yunhui Huang*[a]

[a]State Key Laboratory of Material Processing and Die & Mold Technology, School of Materials Science and Engineering, Huazhong University of Science and Technology, Wuhan 430074, China

[b]School of Energy and Power Engineering, Huazhong University of Science and Technology, Wuhan, Hubei 430074, China.

[c]Zhejiang Funlithium New Energy Technology Co., Ltd.Ningbo, Zhejiang 315201, P. R. China

[d]Department of Physics City, University of Hong Kong, Hong Kong 999077, P. R. China

[e]State Key Laboratory of Silicon and Advanced Semiconductor Materials, School of Materials Science and Engineering, Zhejiang University, Hangzhou, China.
E-mail: thliu@hust.edu.cn, xuhh@hust.edu.cn, huangyh@hust.edu.cn

Methods

Chemicals and materials

Active materials NCM622 or NCM811 or LCO or $LiNi_{0.5}Mn_{1.5}O_4$ powders, Super C65, polyvinylidene fluoride (PVDF), carbon-coated aluminum (Al, 15 μm-thick) foil, Cu foil and Al_2O_3-coated polyethene (PE, 16 μm thick) were purchased from the Guangdong Canrd New Energy Technology Co., Ltd. Anhydrous N-methyl-2-pyrrolidone (NMP), EA and its fluorinated derivatives, TFEA, and 2, 2′-azobis (2-methylpropionitrile) (AIBN) were purchased from Aladdin Reagent (Shanghai) Co., Ltd. $LiPF_6$, EC, DEC and FEC were purchased from DoDoChem. PETEA was purchased from Sigma-Aldrich (Shanghai) Trading Co., Ltd. Li foils (500 μm) were purchased from China Energy Lithium Co., Ltd. EA and its fluorinated derivatives were dried with 4 Å molecular sieves (Sigma–Aldrich) before use.

Preparation of electrodes

Cathodes were prepared by a slurry-coating method with calendaring step. Typically, 80 wt% active materials, 10 wt% Super C65, and 10 wt% PVDF were wetly mixed together in the NMP solvent for 12 h by using a stirrer. And then, the slurry mixture was cast onto a carbon-coated Al foil and then dried at 80 °C for 12 h in a vacuum. The loadings for NCM622, LCO and $LiNi_{0.5}Mn_{1.5}O_4$ cathode active material mass were ~7.5, 6, and 5 mg cm^{-2}. To prepare high loading NCM622 cathode (3 and 4.4 mAh cm^{-2}), active materials, Super C65, and PVDF were mixed with a weight ratio of 90: 5: 5. The prepared cathodes were punched into 8 mm discs and stored in glove box for use.

Preparation of F-Gel electrolyte

Electrolytes were prepared and stored in an argon gas-filled glovebox (H_2O < 0.1 ppm, O2 < 0.1 ppm). To prepare F-Gel electrolyte, TFEA monomer, EA-2F, and FEC solvent were added into a glass bottle with a volume ratio of 1: 7.2: 1.8 and stirred for 30 min. Then 1 M $LiPF_6$, 0.5 wt% AIBN, and 1.5 wt% PETEA were added in to the above solution and stirred for 10 min to get the precursor solution. Subsequently, the glass

bottle was heated at 60 °C for 3 h to obtain F-Gel electrolyte. CR2032 coin cells were assembled in an Ar-filled glovebox using Al_2O_3-coated PE separator, Li metal anode, and cathode. The above precursor solution was injected into the separator (40 µL) and then the assembled coin cells were transferred to the oven and heated at 60 °C for 3 h to ensure the complete polymerization. Hence, the quasi-solid-state LMBs were obtained. The Li||NCM622, Li||NCM811 and Gr/SiO||NCM811 pouch cells were injected with electrolytes before sealing.

Electrochemical tests

All coin and pouch cells were measured on a Neware testing system at 25, –20, and –40 °C. The ionic conductivities of F-Gel electrolyte and C-LE were measured by a Leici (DDB-303A) electrical conductivity meter (INESA Group Co., Ltd.). Li||Cu cells were measured with the method proposed by Adams et al[1]. Prior to the test, a condition cycle was carried out on all the cells, where 5 mAh cm^{-2} of Li was deposited onto the Cu foil at 0.5 mA cm^{-2}, and then fully stripped to 1V to form the SEI before CE testing. During testing 5 mAh cm^{-2} was first deposited followed by 10 cycles of 1 mAh cm^{-2} plating and stripping before finally stripping all Li to 1 V. The CE was calculated by dividing the total stripped capacity by the total plated capacity. The exchange current density was calculated based on the Tafel equation measured at –20 °C at a scan rate of 0.1 mV s^{-1} from –0.25 to 0.25 V. LSV test were conducted on Li||Al cells with a scan rate of 0.1 mV s^{-1}. The transference number (t_{Li+}) of the electrolytes was examined *via* Li/Li symmetric cells, where a polarization voltage of 10 mV was applied.[2] To investigate the reduction stability of F-Gel electrolyte, Li||Li symmetric cells were assembled and tested at RT and –20 °C.

Li||NCM622 coin cells were cycled in the voltage range of 3.0–4.4 V (1 C= 200 mAh g^{-1}) or 3.0–4.6 V (1 C= 220 mAh g^{-1}) at 0.1 C for the initial two activation cycles. LMBs pouch cells were cycled in the voltage range of 3.0–4.3 V or 3.0–4.4 V at 0.1 C for the initial two activation cycles. The cycling performance of the pouch cells was

tested under a fixing device to provide a clamping torque of 300 N cm. Electrochemical impedance spectroscopy of Li||Li and Li||NCM622 batteries (at the end of the discharge) was conducted on a CHI660e electrochemical workstation (Chenhua Instrument Co., Shanghai, China) with a frequency from 10^6–1 Hz at an amplitude of 10 mV.

Material characterizations

Fourier Transform InfraRed (FT-IR) spectrum was collected from Nicolet iS50R (Thermo Scientific) in the range of 400 to 4000 cm^{-1}. The data were fitted with Peakfit software. Raman spectroscopy investigations were conducted by a Micro-laser confocal Raman spectrometer (Horiba LabRAM HR800, France) at RT. Differential scanning calorimetry (DSC) analyses of polymer electrolytes were obtained in a DSC2500, TA equipment. The samples were heated from −90 °C to 90 °C in N_2 atmosphere at a heating rate of 5 °C min^{-1}. ^{7}Li and ^{19}F NMR spectroscopy experiments were performed on Bruker Ascend 500WB (11.7 T) equipped with a 4 mm double resonance HX probe. The ^{7}Li NMR spectra were recorded with a 90° pulse length of 6.5 μs, a recycle delay of 5 s, and 32 scans. The shift of ^{7}Li was referenced to 1 M LiCl (aqueous solution) at 0 ppm. The ^{19}F NMR spectra were recorded with a 90° pulse length of 5.5 μs, a recycle delay of 2 s, and 32 scans. The shift of 19F was referenced to 0.2 M KF (aqueous solution) at 0 ppm. Spin lattice relaxation time (T1) of ^{7}Li was measured using an inverse-recovery pulse sequence with a 90° pulse length of 3.0 μs

For postmortem analyses, Li||Cu and Li||NCM622 coin cells (after 50 cycles at RT and −20 °C) were disassembled to collect the Li foils or the NCM cathodes. X-ray diffraction was performed on an X-ray powder diffractometry (PANalytical X'pert PRO-DY2198, Holland) operating at 40 kV and 40 mA with Cu Kα radiation (λ=0.15406 nm) in the range of 10°~60° with a step size of 0.013°. The morphologies of the deposited Li, cycled lithium anode and NCM622 cathode were investigated by scanning electron microscope SEM (FEI, Quanta650 FEG). X–ray photoelectron spectra (XPS) was acquired from a Thermo Scientific ESCALAB Xi+. The cycled lithium anode and polymer electrolytes were sealed in a sample transfer tool under Ar

environment. All XPS test narrow scan data are calibrated with C 1s 285.0 eV. XPS peak 4.1 was used to analyze and fit the peaks. In order to probe the distribution of fragments in SEI and CEI, the time-of-flight secondary ion mass spectrometry (ToF-SIMS) test was conducted on the cycled lithium anode and NCM622 cathode using ToF-SIMS 5 iontof, PHI NanoTOFII with a 30 keV bismuth liquid metal ion source. The analysis area was 300 μm × 300 μm. Depth profiles were obtained by sputtering ion beams of Ar^+ (1 keV) on a 100 μm × 100 μm square with a sputtering rate was 0.1 nm s^{-1}. TEM samples were harvested from the disassembled NCM222 electrodes and a secondary particle of NCM622 was selected randomly to characterize the morphology and microstructure by using TEM (JEM-2100f). The transitional metals elemental distributions of lithium anode sample were evaluated with a micro-focusing X-ray fluorescence (u-XRF, Bruker Inc.) map. The Young's modulus distributions of CEI were detected by Atomic Force Microscope (Jupiter XR, Oxford Instruments Asylum Research, Inc).

Molecular dynamic calculations

The molecular dynamics (MD) simulations were performed using the Large-scale Atomic/Molecular Massively Parallel Simulator (LAMMPS)[3]. The interatomic interactions of organic molecules were described using the polymer consistent force field plus (PCFF++) provided by the MedeA package from Materials Design, Inc. Although PCFF++ force field is commonly adopted to model organic compounds, it uses a 9–6 Lennard-Jones potential. In this simulations, a 12–6 Lennard-Jones potential was used instead according to Kumar *et al.*'s study[4], with a cutoff radius of 12 Å. For PF_6^-, the bond interaction potentials are derived from Takeuchi et al.'s research[5]. The charges of lithium ion and PF_6^- were scaled down to $\pm 0.8|e|$ to mimic polarization and charge transfer effects[6]. The long-range electrostatic interactions were treated by the Particle-Particle Particle-Mesh (PPPM) method with a cutoff radius of 10 Å for the Coulomb interactions. The ions and molecules were randomly placed in the simulation box based on the molar ratio. For all systems, the time step was fixed at 1.0 fs. After relaxation to thermal equilibrium, the simulation boxes were respectively equilibrated

at the temperature of 253 K and 298 K as well as the pressure of 1.0 bar for 5.0 ns in the NPT ensemble for optimizing the box size. Subsequently, a 5.0 ns MD simulation in the NVT ensemble was performed, where the last 4.0 ns was adopted for the radial distribution functions (RDFs) analysis. Following this, another 10.0 ns MD simulation in NVT ensemble was conducted for the mean-squared displacement (MSD) analysis. The MSD results were averaged from 10 independent MD simulations using different initial velocity distribution. Finally, snapshots were recorded every 4000 time steps from a 5.0 ns MD simulation in the NVT ensemble to calculate the coordination number of lithium ions. Focusing on the solvation structures, we counted oxygen, fluorine, and phosphorous atoms within a distance of 2.4, 2.4, and 4.0 Å, respectively.

DFT Calculation

The LUMO and HOMO energy level, electrostatic potential maps, and binding energies were calculated by the Gaussian 16 package. Geometry optimization was based on the 6-31+G(d) level of theory. After geometry optimization, 6-311++G(d, p) level of theory was used to calculate single-point energy. Binding energies of the $Li^+(Solvent)x$ complexes were calculated after geometry optimizations, in which the full complexes were optimized with and without Li^+, representing their separation at an infinite distance. The binding energy (E_b) was calculated as: $E_b = E_{Li^+(solvent)x} - (E_{Li^+} + E_{x(solvent)})$. The electrostatic potential involved in the analyses was evaluated using Multiwfn based on the highly effective algorithm proposed by Lu et al[7, 8].
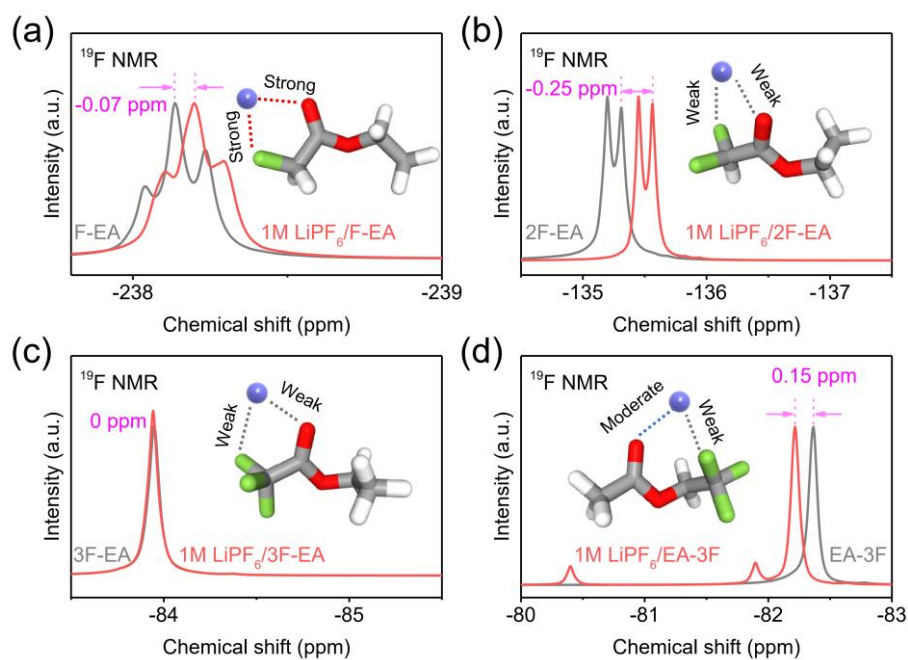
Fig. S1 ^{19}F-NMR spectroscopy of pure solvents and the corresponding electrolytes. (a) F-EA and 1 M LiPF$_6$/F-EA, (b) 2F-EA and 1 M LiPF$_6$/2F-EA, (c) 3F-EA and 1 M LiPF$_6$/3F-EA, (d) EA-3F and 1 M LiPF$_6$/EA-3F.

Note: An upfield ^{19}F peak shift was observed when LiPF$_6$ was dissolved in F-EA or 2F-EA solvent. By contrast, ^{19}F signal stayed at almost the same position for 3F-EA before and after dissolving LiPF$_6$ while the ^{19}F signal of EA-3F showed downfield shift, confirming that fully fluorinated –CF$_3$ group did not strongly interact with Li$^+$ ions.[9-11]
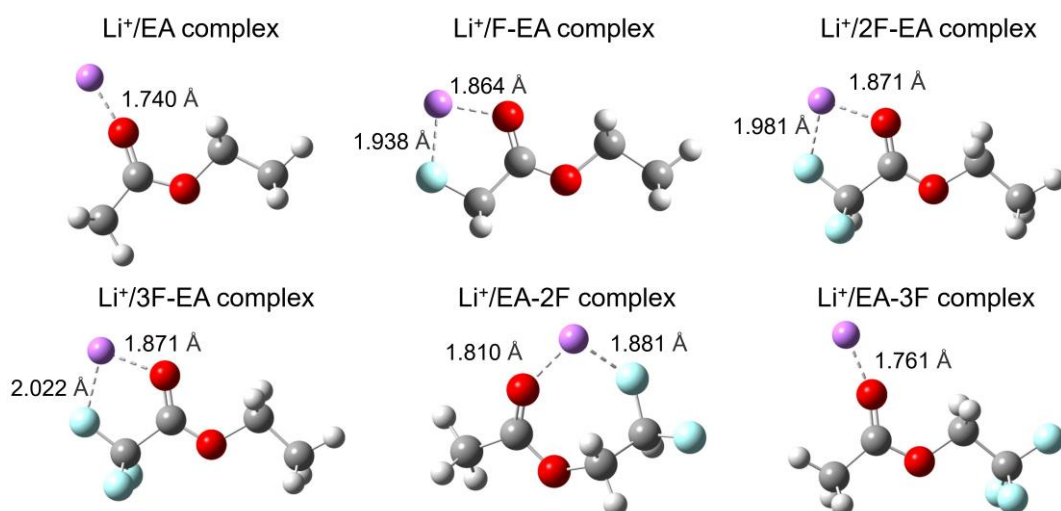
Fig. S2 Coordination structures of Li$^+$/solvent complexes. Color scheme of atoms: Li-purple, C-gray, H-white, O-red, F-light blue.

DFT was used to determine optimized binding configurations between Li$^+$ and each type of solvent mole. It is found that the Li$^+$ shows stronger interaction with ethoxy side partially fluorinated ethyl acetate ($-OCH_2CF_2H$) compared to monofluoride ($-CFH_2$), trifluoro ($-CF_3$) and methyl side difluoro ($-CF_2H$) counterparts indicated by the shorter Li–F distance of 1.881 Å. Such a stronger Li–F interaction enables $-OCH_2CF_2H$ group to enter Li$^+$ solvation structure and reduces the Li–O interaction intensity, thus accelerating Li$^+$ de-solvation process at low temperature.
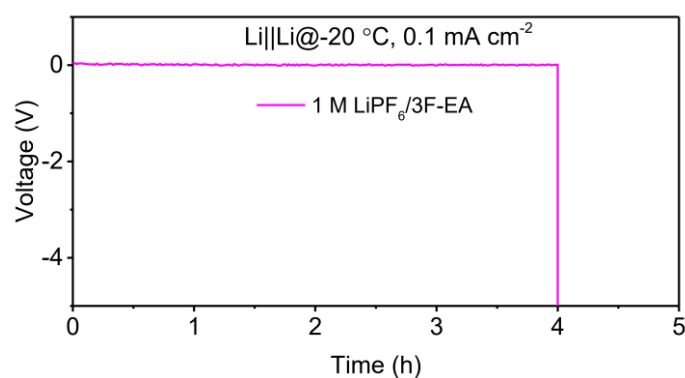
Fig. S3 Cycling performance of Li‖Li symmetric cells with 1 M LiPF$_6$/3F-EA electrolytes at a current density of 0.1 mA cm^{-2} at –20 ºC.

| EA | F-EA | 2F-EA | 3F-EA | EA-2F | EA-3F |
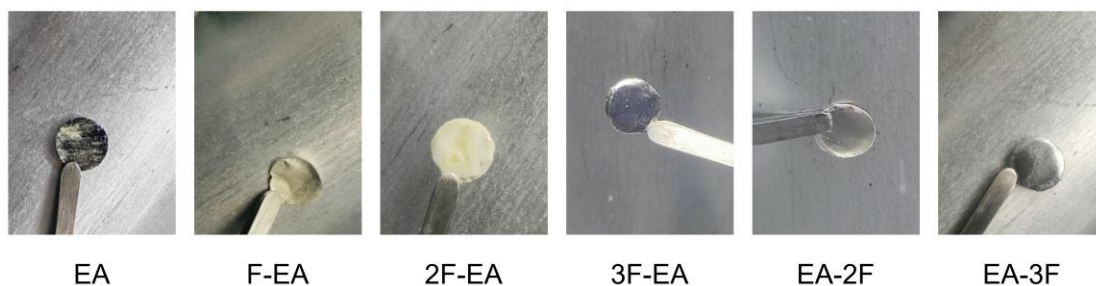
Fig. S4 Chemical stability of the fluorinated ethyl acetates pure solvent with Li metal tested through immersing Li metal in the pure solvent for 3 days.

The chemical compatibility of fluorinated ethyl acetates with lithium anode was further assessed by immersing Li metal in pure solvent for 3 days. The surface of the Li sheet retained a metallic luster for EA-2F and 3F-EA, whereas a pale-yellow color was observed on the lithium anode immersed in EA, F-EA, 2F-EA and EA-3F. The discrepancy compatibility can be explained by the heightened reactivity of α-hydrogen in fluorinated carboxylate solvents with Li metal. The resultant reaction products have poor film-forming properties[12], failing to passivate the lithium anode. Notably, 3F-EA presents high chemical stability towards lithium anode because of the lack of α-hydrogen.
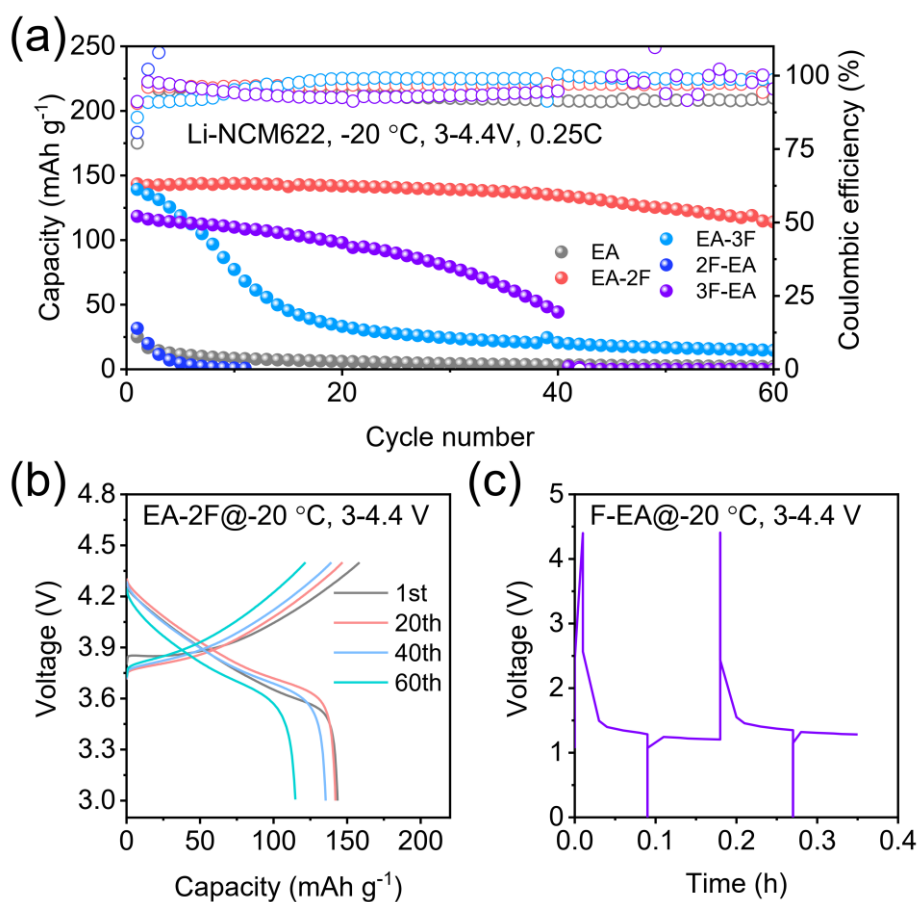
Fig. S5 (a) Long-term cyclability of Li‖NCM622 cells with different fluorinated solvent molecules at –20 °C. Charge–discharge voltage profiles of the Li‖NCM622 cells with (b) EA-2F-based electrolyte and (c) F-EA-based electrolyte.

The Li‖NCM622 battery with EA-2F based electrolyte delivers a high capacity retention over 80% after 60 cycles at 0.25 C rate under –20 °C (3-4.4 V). Mover, the CEs exceed 97% after 30 cycles and remain stable, indicating EA-2F solvent molecules has high stability to lithium anode and NCM622 cathode. By contrast, the Li‖NCM622 batteries with EA or other fluorinated solvents based electrolytes present poor cycling performance and fluctuated CEs, suggesting the solvent molecules decompose during cycling. Besides, the discharge capacity of Li‖NCM622 battery with F-EA-based electrolyte is nearly zero due to the severe side reaction between electrode and F-EA solvent.
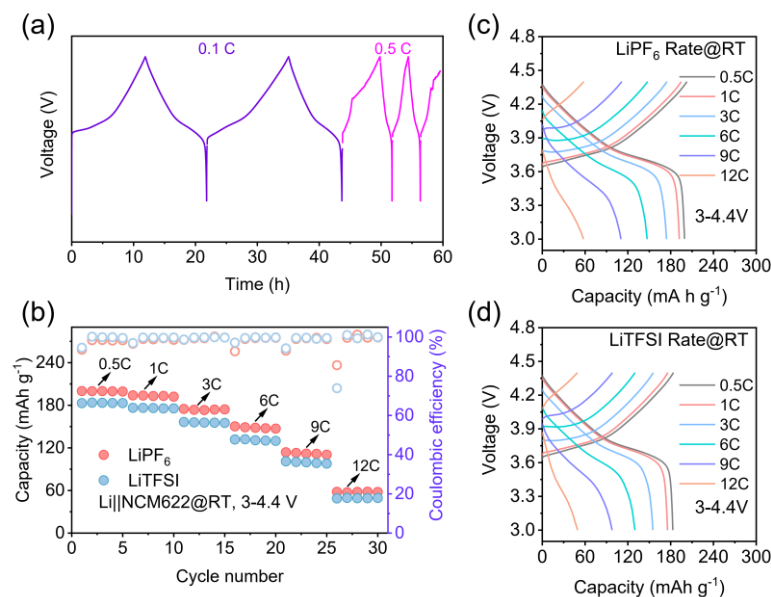
Fig. S6 (a) Galvanostatic charge and discharge plots of the Li‖NCM622 cell with LiFSI-based electrolyte at room temperature. (b) Rate performance of Li‖NCM622 cells with LiPF$_6$ and LiTFSI based electrolytes at room temperature. Charge–discharge voltage profiles of the Li‖NCM622 coin cells with (c) LiPF$_6$-based electrolyte and (d) LiTFSI-based electrolyte at room temperature.

A series of experiments were conducted to investigate the effect of lithium salt on the rate and cycling performance of battery with fluorinated electrolyte (1M lithium salt in EA-2F: FEC= 8: 2 by volume). When LiFSI was used as lithium salt, the Li‖NCM622 cell presented a lower CEs due to LIFSI engendering corrosion for aluminium (Al) current collectors, causing electron pathways to disconnect between the active material and Al current collector and leading to the rapid capacity degradation of battery under high cut-off voltages (Fig. S6a). As a comparison, the LiPF$_6$ and LiTFSI based electrolytes showed higher and stable CEs at room temperature (Fig. S6b-d).

11
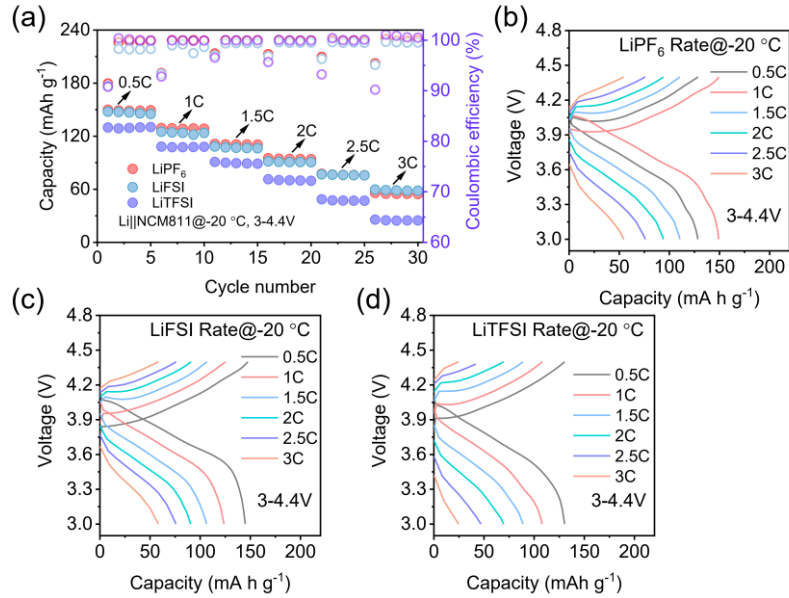
Fig. S7 (a) Rate performance of Li‖NCM811 cells with LiPF₆, LiFSI, and LiTFSI based electrolytes at –20 °C. Charge–discharge voltage profiles of the Li‖NCM811 coin cells with (b) LiPF₆-based electrolyte, (c) LiFSI-based electrolyte and (d) LiTFSI-based electrolyte.

The Li‖NCM811 rate performance at –20 °C revealed that LiPF₆-based electrolyte showed high discharge specific capacities and CEs while LiTFSI-based electrolyte delivered low discharge specific capacities (Fig. S7). In addition, the electrolyte based on LiFSI displayed the lowest CEs among the three lithium salts.
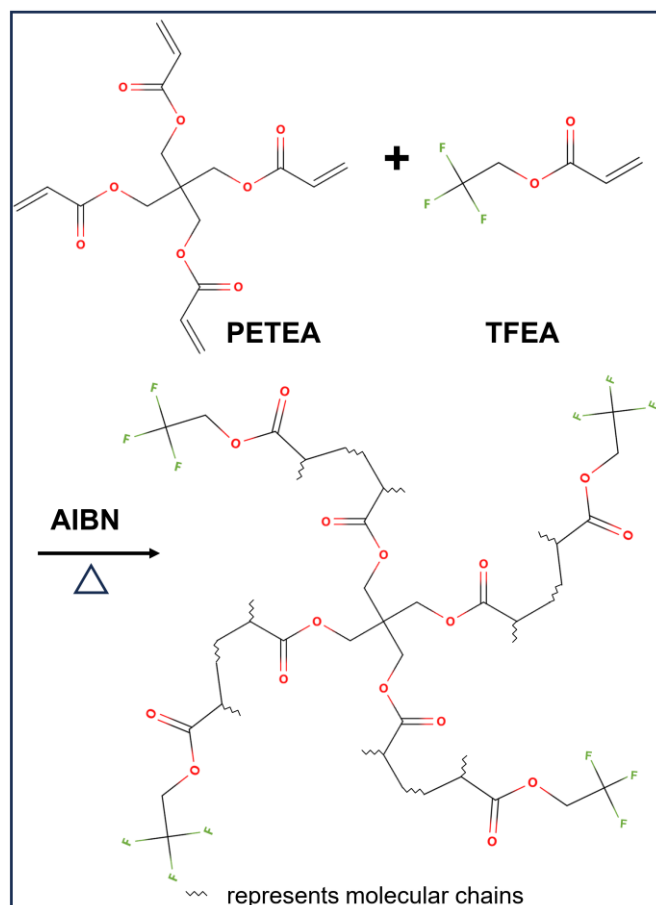
Fig. S8 *In situ* co-polymerization mechanism of TFEA and PETEA monomers in liquid electrolyte.
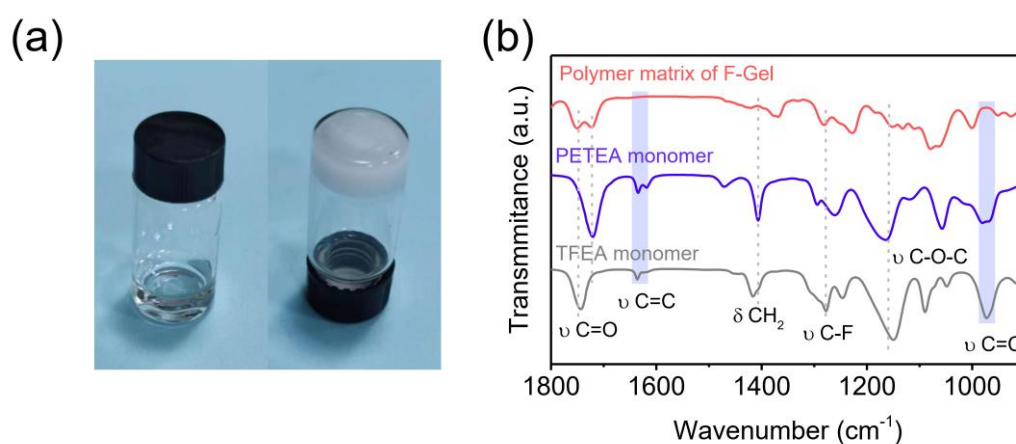
Fig. S9 (a) Optical images of the precursor solution (left) and the corresponding F-Gel electrolyte (right) after copolymerization. (b) FT-IR spectra of the TFEA, PETEA, and the polymer matrix of F-Gel.
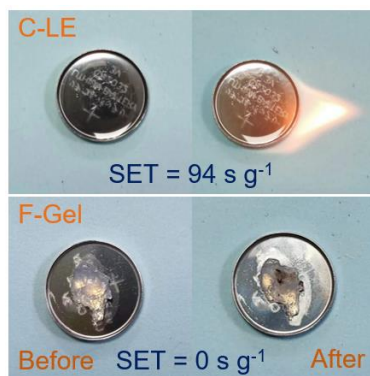
Fig. S10 Combustion tests of C-LE and F-Gel electrolyte.

Fig. S11 Leakage tests of F-Gel (upper panels) and 1 M LiPF$_6$ in EA-2F: FEC fluorinated electrolyte (lower panels).

Leakage tests of fluorinated electrolyte (1 M LiPF$_6$ EA-2F: FEC) and F-Gel electrolyte were conducted. 1 g fluorinated electrolyte and 1 g precursor solution of F-Gel were sealed into Al plastic packages (75 mm × 70 mm), respectively, to simulate liquid leakage in pouch cells. Then the latter was heated at 60 ℃ for 3 h to obtain F-Gel electrolyte. After that, a small notch was cut in each package, and then the packages were squeezed for15 s under a 1 kg weight. The liquid electrolyte package showed a 13 wt% leakage, while F-Gel was absolutely leak-free. Subsequently, the packages were further hung for 5 min. The weight loss was 61.5 % for the liquid electrolyte while that

of F-Gel was 0 %, demonstrating the superior resistance of F-Gel electrolyte against liquid leakage.
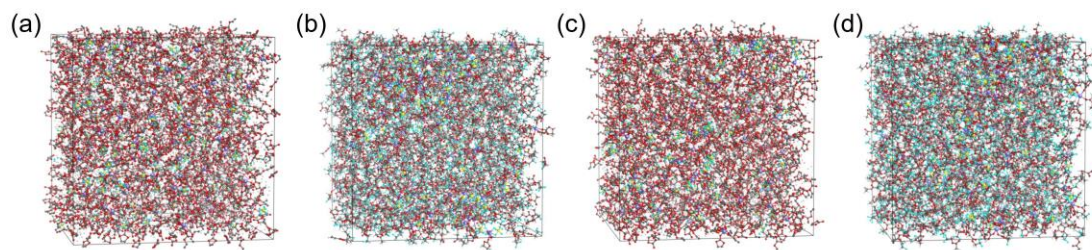
Fig. S12 Molecule dynamics (MD) simulation snapshots of (a) C-LE at RT, (b) F-Gel electrolyte at RT, (c) C-LE at –20 ºC, (d) F-Gel electrolyte at –20 ºC.
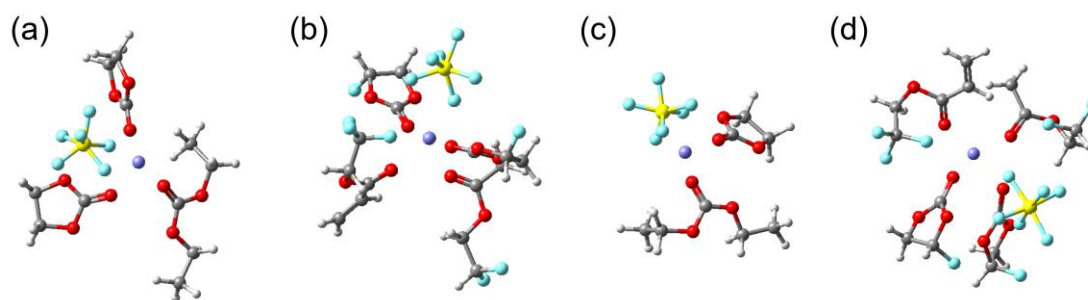
Fig. S13 The representative solvation structures of the primary Li^+ solvation shell of (a) C-LE at RT, (b) F-Gel electrolyte at RT, (c) C-LE at –20 ºC, (d) F-Gel electrolyte at –20 ºC. Color scheme of atoms: Li-purple, C-dark gray, H-light gray, O-red, F-cyan, and P-yellow.

The representative microstructures of the first solvation sheath (within 2.4 Å) were extracted and displayed in Fig. S13. Both electrolytes can witness solvent molecules and anions interacting with Li^+ ions in the first solvation shell at RT and –20 ºC. It is worth noting that the coordination of Li^+ to F atom and O atom of EA-2F solvent molecule can be observed in F-Gel electrolyte owing to the moderate solvation affinity of solvents *via* fluorinated regulation.
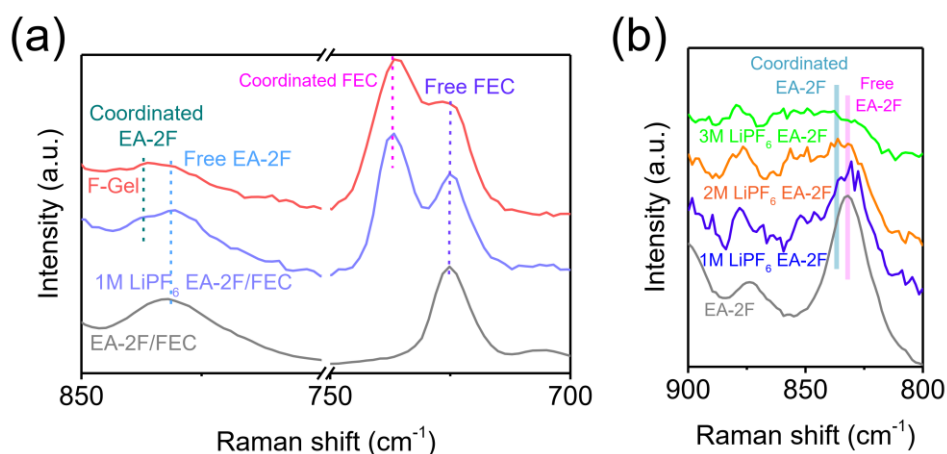
Fig. S14 Raman spectra of (a) EA-2F/FEC mixture, 1 M LiPF$_6$ EA-2F/FEC and F-Gel electrolytes, (b) 1 M LiPF$_6$ EA-2F, 2 M LiPF$_6$ EA-2F and 3 M LiPF$_6$ EA-2F.

Raman spectra was measured to characterize the coordination environment in the electrolyte. It is seen that in the mixture of EA-2F: FEC (1: 1 by volume), peaks at around 725 cm^{-1} were recorded (assigned to free FEC) and one at about 831 cm^{-1} corresponding to the free EA-2F molecule. After dissolving 1 M LiPF$_6$ into the mixture, the peak intensity of free solvent molecules diminished accompanying the appearance of new bands at about 737 cm^{-1} (Li$^+$-coordinated FEC), 837 cm^{-1} (Li$^+$-coordinated EA-2F)[13]. With the addition of TFEA, the peak intensity of Li$^+$-coordinated FEC and EA-2F increased, which verifies that more fluorinated solvent molecules are coordinated with Li ions in the solvation sheaths.
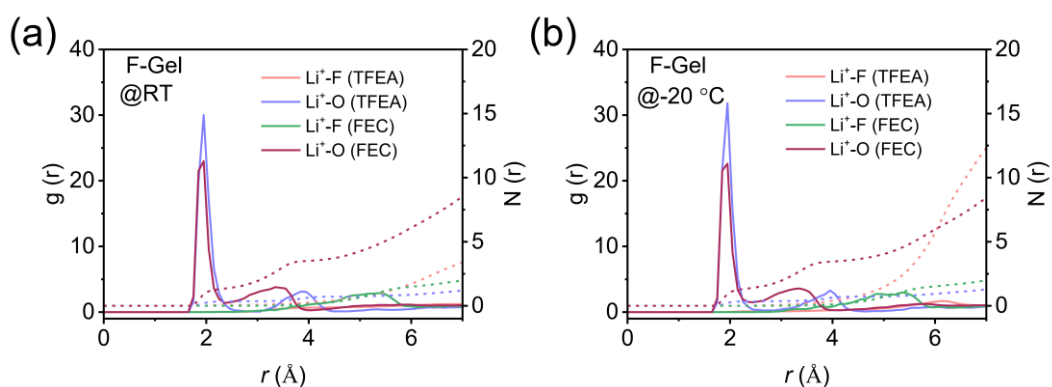
Fig. S15 Radial distribution functions (RDFs) and coordination numbers of (a) F-Gel electrolyte at 25 ºC, (b) F-Gel electrolyte at –20 ºC.

At RT, the solvation radiuses of FEC and TFEA solvent molecules in F-Gel electrolyte were 1.91 and 1.94 Å, which were comparable with that of EA-2F but larger than that of EC solvent molecules in C-LE, indicating a moderate solvation structure. With a low operation temperature of –20 ºC, the solvation structure of F-Gel electrolyte showed negligible change and maintain a moderate solvation structure.
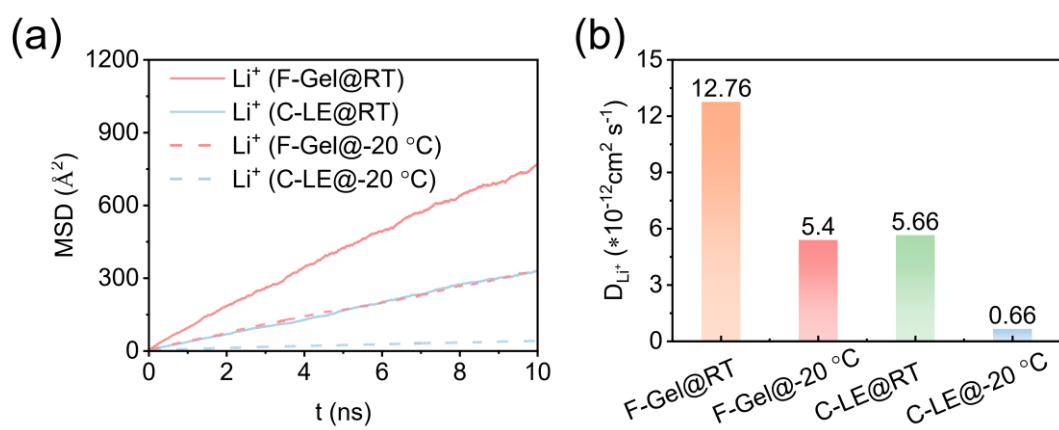
Fig. S16 (a) Mean square displacement versus simulation time for Li$^+$ in C-LE and F-Gel electrolyte at RT and –20 ºC. (b) The results of Li$^+$ diffusion coefficient based on 20 MD simulations in the corresponding electrolytes and temperatures.

The diffusion coefficients of Li$^+$ ions are calculated to be 12.76×10^{-12} and 5.4×10^{-12} cm^2 s^{-1} for F-Gel electrolyte at RT and –20 ºC, which are much larger than that of C-LE due to the moderate Li−O and Li−F interaction between Li$^+$ and EA-2F solvent.
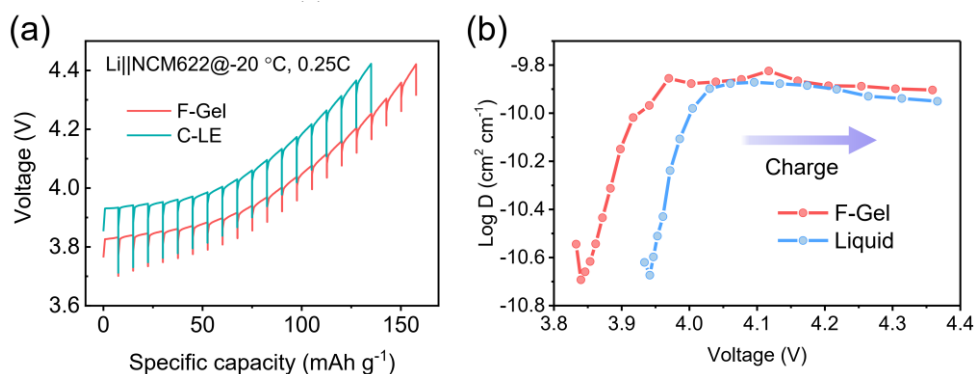
Fig. S17 (a) GITT plots of the Li‖NCM622 cell at –20 °C with both electrolyte in the charge process. (b) The corresponding Li$^+$ diffusion coefficient.

The galvanostatic intermittent titration technique (GITT) results indicate that the voltage polarization of F-Gel electrolyte is significantly lower than that of C-LE due to the enhanced Li$^+$ de-solvation process. In addition, the Li$^+$ diffusion coefficient of F-Gel electrolyte is also much larger than that of C-LE, further demonstrating that a fast Li$^+$ diffusion in the NCM622 cathode at –20 °C.
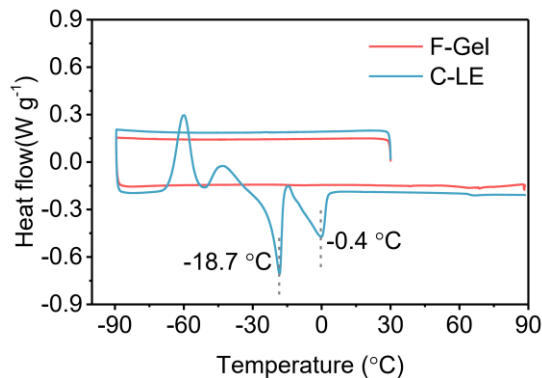
Fig. S18 DSC cooling and heating curves of both electrolytes.
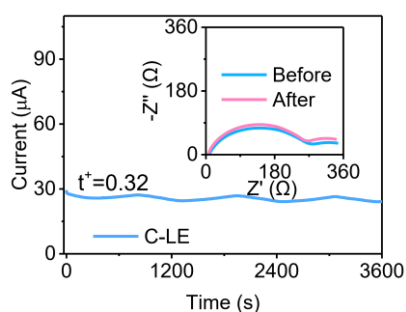
Fig. S19 Chronoamperometry for Li$^+$ transference number (t_{Li+}) of C-LE.
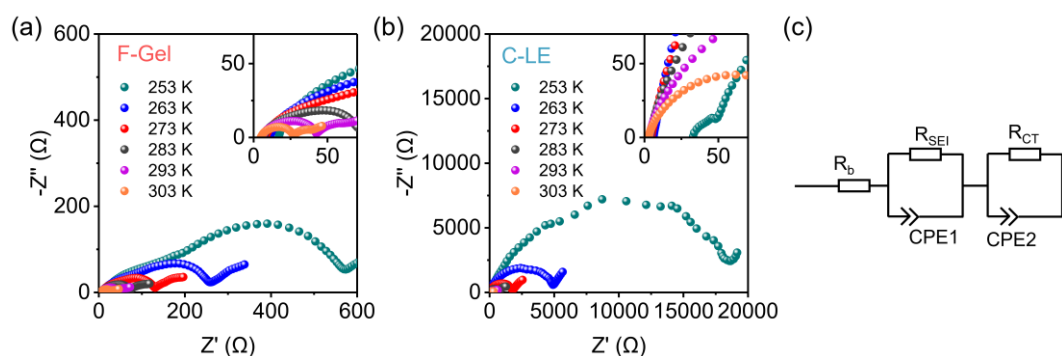
Fig. S20 Nyquist plots of cells using (a) F-Gel electrolyte and (b) C-LE. (c) The equivalent circuit model and the corresponding Nyquist plot of Li‖Li symmetric cells. Note: R_b represents the bulk resistance, reflecting the resistance of electrodes, electrolyte, and separator. The semi-circle of R_{SEI} in the high-middle frequency range represents the resistance of Li$^+$ transport through the SEI, while the semi-circle of R_{CT} in the low frequency range represents the de-solvation resistance of Li$^+$ before it enters the SEI.
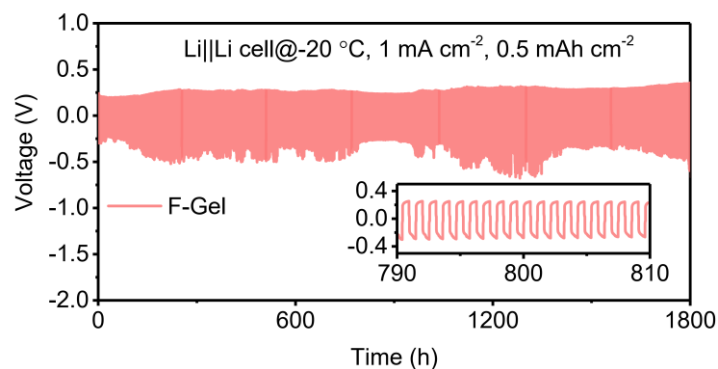
Fig. S21 The long-term cycling performance of Li‖Li symmetric battery with F-Gel electrolytes at –20 ºC.
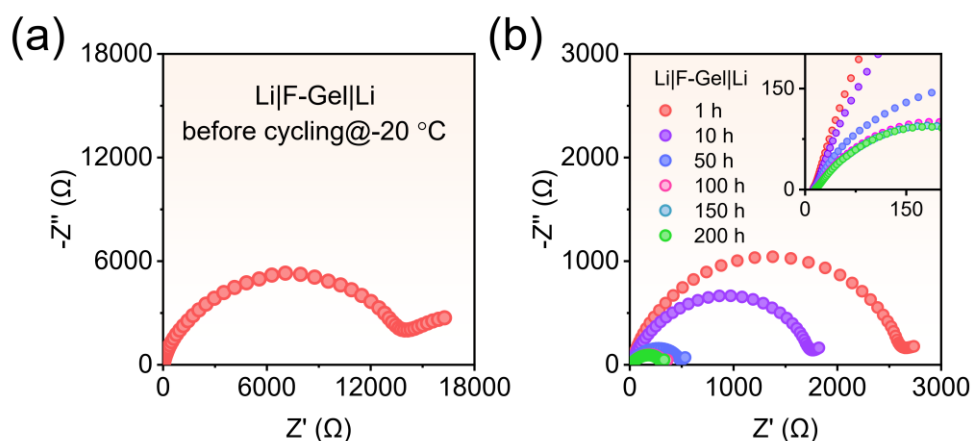
Fig. S22 (a) The EIS plot of the Li|F-Gel|Li cell before cycling. (c) The EIS plots of the Li|F-Gel|Li cell after different cycling time.
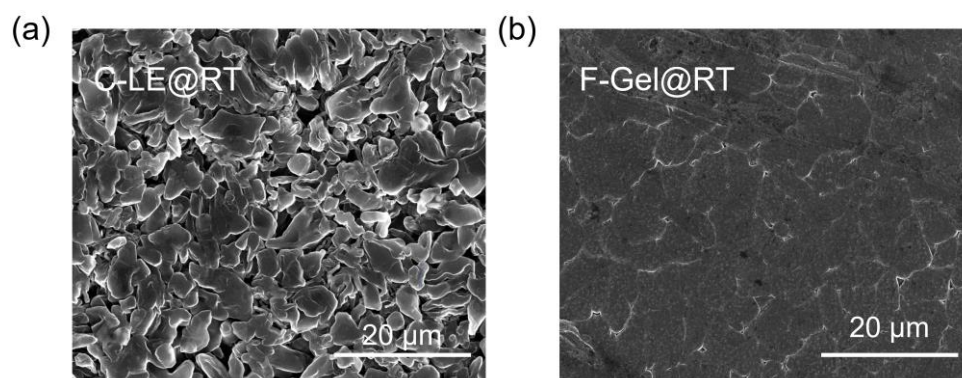
Fig. S23 SEM images illustrating Li deposition morphologies in Li||Cu cells with (a) C-LE and (a) F-Gel electrolyte under an areal capacity of 5 mAh cm^{-2} at RT.

The scanning electron microscopy (SEM) images of C-LE system at RT are shown in Fig. S23, where deposited Li chunks are apparently distinguished with a diameter of 3~10 μm. As a comparison, the plating Li employing F-Gel electrolyte shows a compact morphology with aggregated large particles at RT.
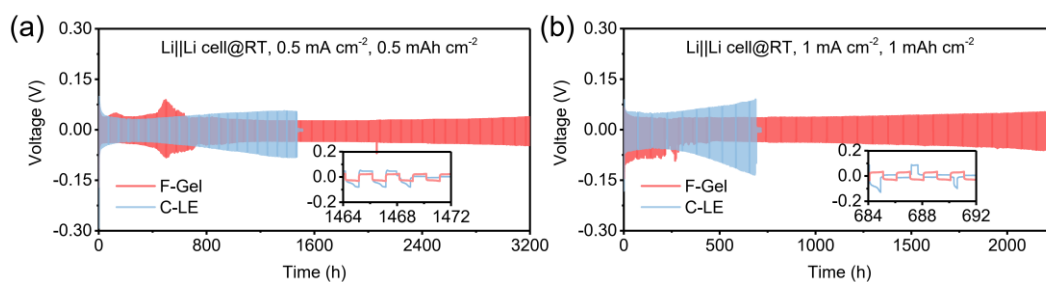
Fig. S24 The long-term cycling performance of Li||Li symmetric batteries with both electrolytes at RT.

At RT, the assembled Li||Li symmetric cells with C-LE experience a continuously increased overpotential during the initial stage, followed by a sudden short-circuit due to the lithium-dendrite growth. Meanwhile, the Li|F-Gel|Li symmetric cells deliver stable cycling performance over 3200 and 2250 h at a current density of 0.5 and 1 mA cm^{-2} at RT, respectively.
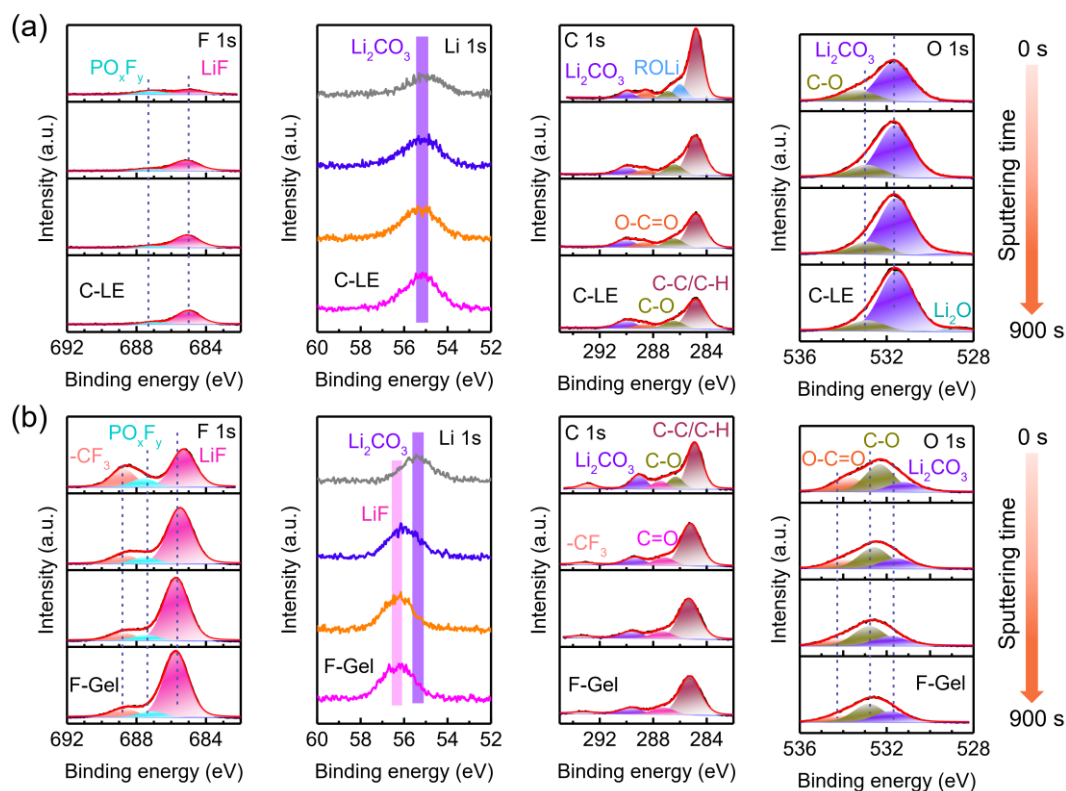
Fig. S25 (a-b) XPS depth profiles of F 1s, Li 1s, C 1s and O1s spectra obtained from the cycled Li anode collected from (a) Li|C-LE|NCM622 and (b) Li|F-Gel|NCM622 cells at RT.

The XPS spectra from C-LE show that the SEI components on lithium anode differ significantly from those in the F-Gel electrolyte. For liquid electrolyte, a weak LiF peak and a strong Li_2CO_3 peak are observed as reflected in the F 1s, Li 1s and O 1s spectra. Besides, the high portion organic specie in outer surface of SEI represents the continuous decomposition of solvent in Li|C-LE|Li cells while the SEI constitution for Li|F-Gel|Li cell is relatively stable during the etching process.
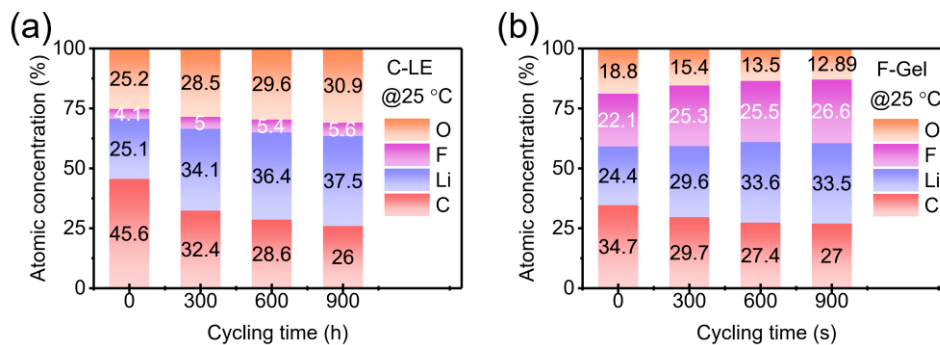
Fig. S26 Elemental portions by XPS of cycled Li metal at RT in (a) C-LE and (b) F-Gel electrolyte.

The relative elemental portions of SEI at different depths are collected in Fig. S26. Compared with C-LE, a lower C element content is detected in the C-E, suggesting the oxidation of solvent molecules is suppressed. For both electrolytes, Li element accounts for a large portion of the SEIs. Besides, C-LE shows a low portion of F element and a high portion of O element. In contrast, for the F-Gel system, it maintains a high portion of F element and a low portion of O element during the etching process, which is able to suppress lithium-dendrite growth.
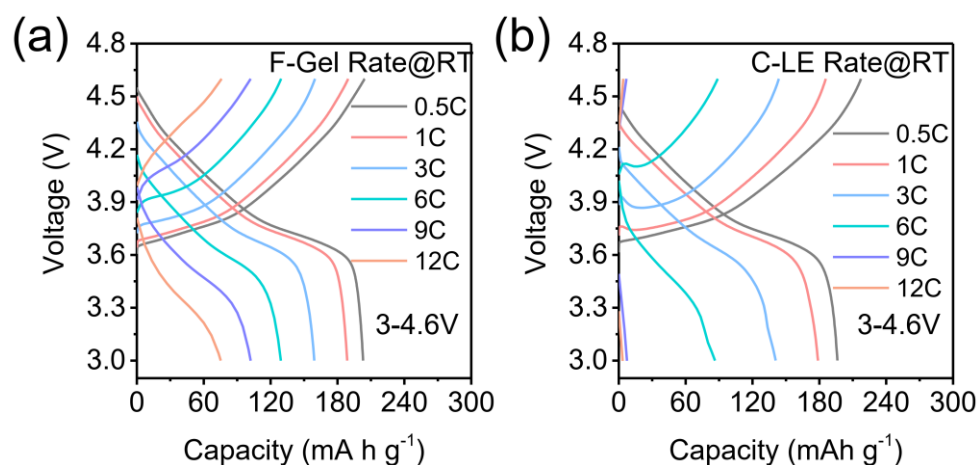
Fig. S27 Charge–discharge voltage profiles of the Li‖NCM622 coin cells with (a) F-Gel electrolyte and (b) C-LE at different applied rate and RT.
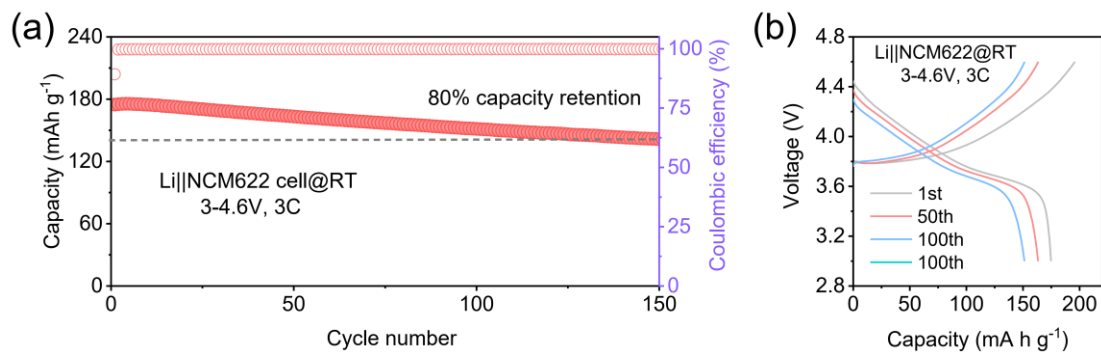
Fig. S28 (a) The long-term cycling performance of Li‖NCM622 batteries at 3C with a high cutoff voltage 4.6 V. (b) The corresponding charge–discharge voltage profiles of the Li‖NCM622 coin cells at 1st, 50th, 100th, and 150th cycles with F-Gel electrolyte.
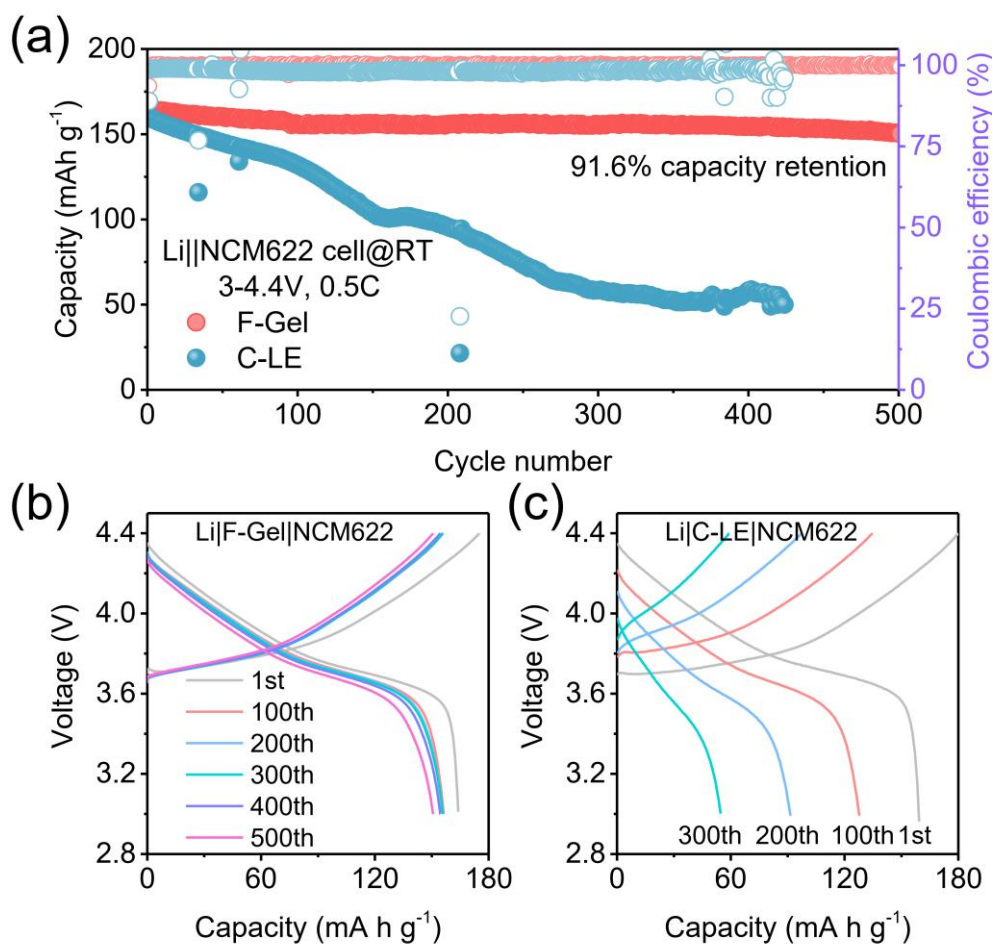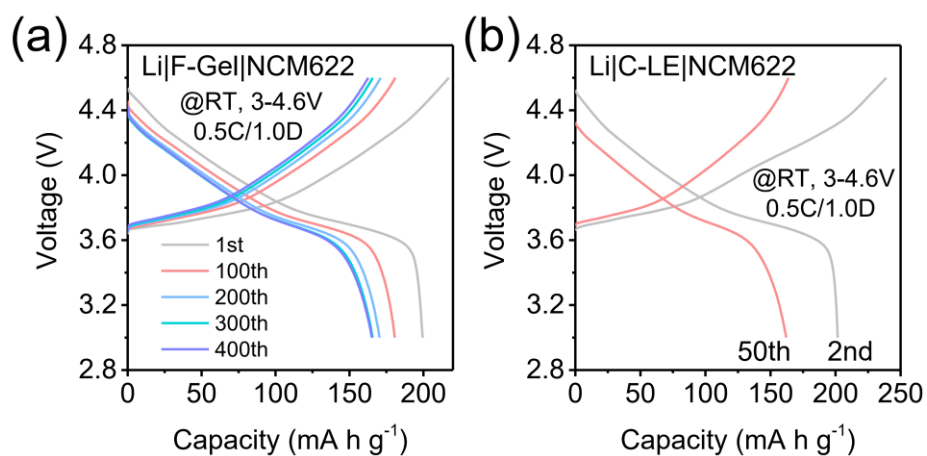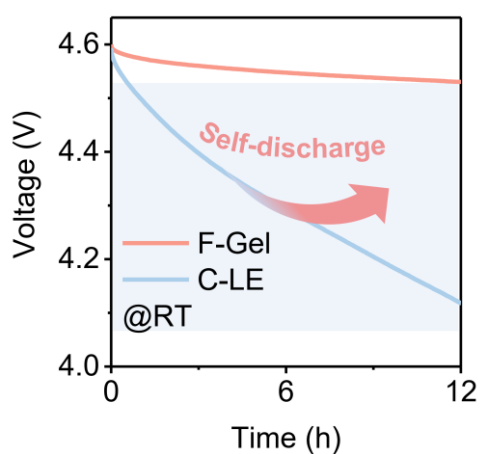

Fig. S29 (a) The long-term cycling performance of Li‖NCM622 batteries with a high cutoff voltage 4.4 V at RT. Charge–discharge voltage profiles of the Li‖NCM622 coin cells with (b) F-Gel electrolyte and (c) C-LE.

Fig. S30 Charge–discharge voltage profiles of the Li‖NCM622 coin cells with (a) F-Gel electrolyte and (b) C-LE at different RT.

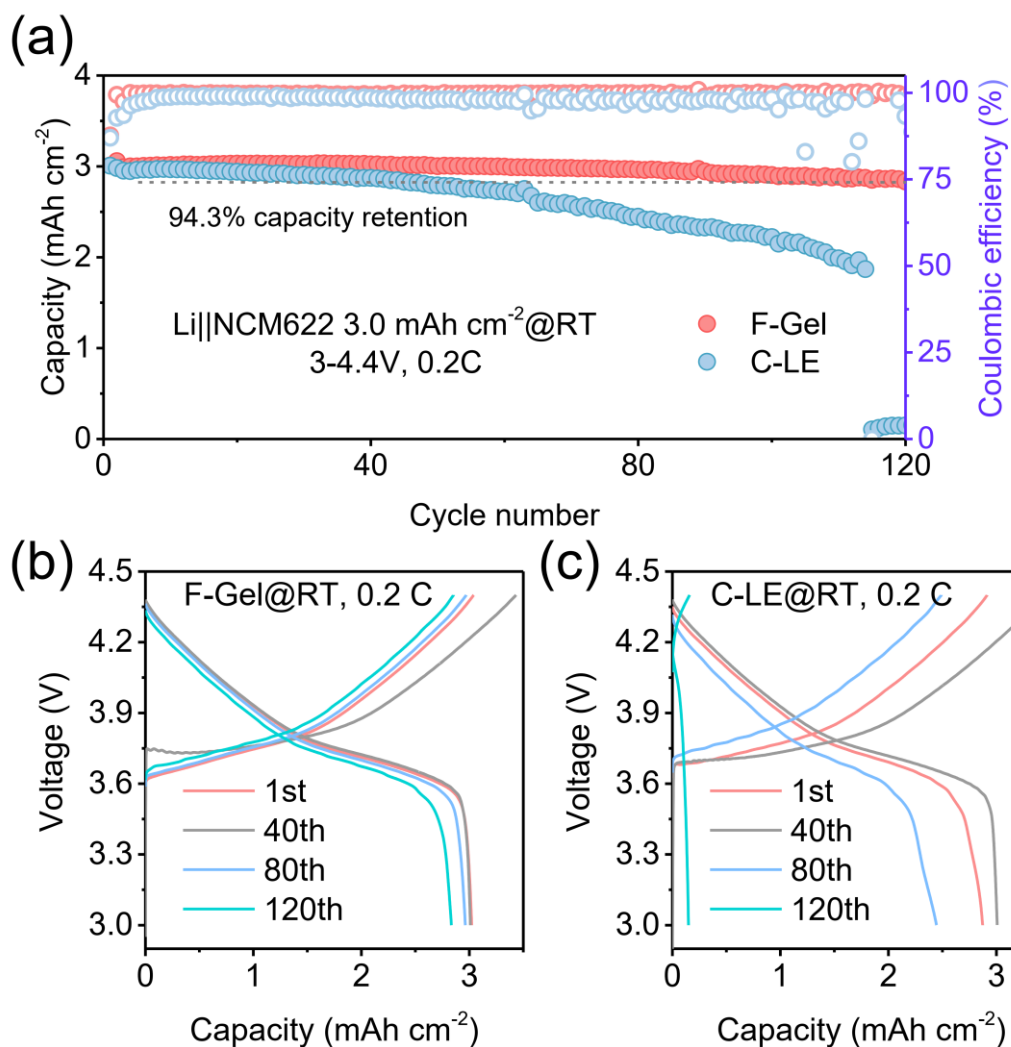**Fig. S31** Self-discharge curves after first charged to 4.6 V and stood for 12 h.

Fig. S32 (a) The long-term cycling performance of Li||NCM622 batteries with both electrolyte under a high areal loading of 3 mAh cm^{-2}. The corresponding charge–discharge voltage profiles of the Li||NCM622 coin cells at 1st, 70th, 80th, 120th cycles with (b) F-Gel electrolyte and (c) C-LE.
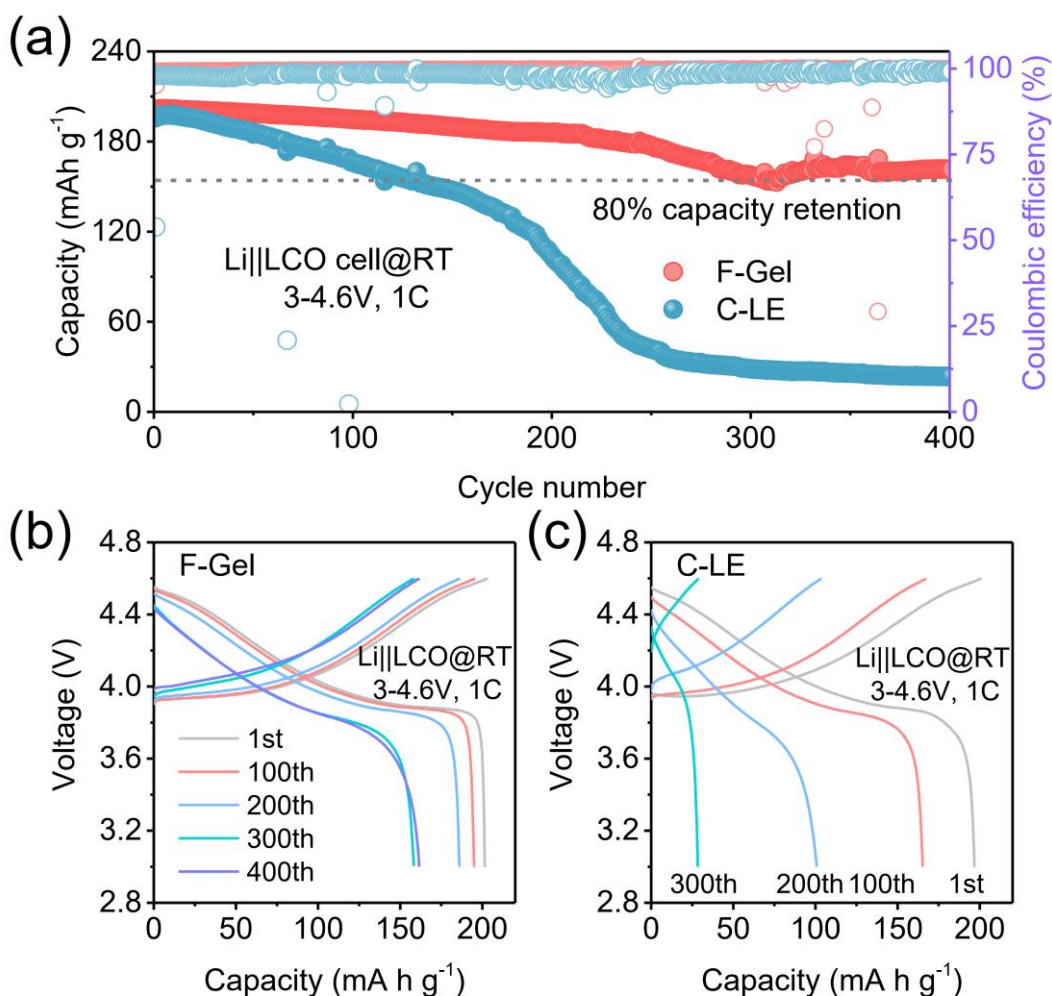
Fig. S33 (a) The long-term cycling performance of Li||LCO batteries with an ultrahigh cutoff voltage 4.6 V at RT. Charge–discharge voltage profiles of the Li||LCO coin cells with (b) F-Gel electrolyte and (c) C-LE.

At a high current density of 1 C, the Li|F-Gel|LCO (1.2 mAh cm^{-2}) cell displays a high capacity retention of 80% over 400 cycles with a 4.6 V cutoff-voltage at RT. As a comparison, the Li|C-LE|LCO cell shows a fast degradation accompanied by an evident smaller Coulombic efficiency attributed to the severe side reactions at high current density and high cut-off voltage.
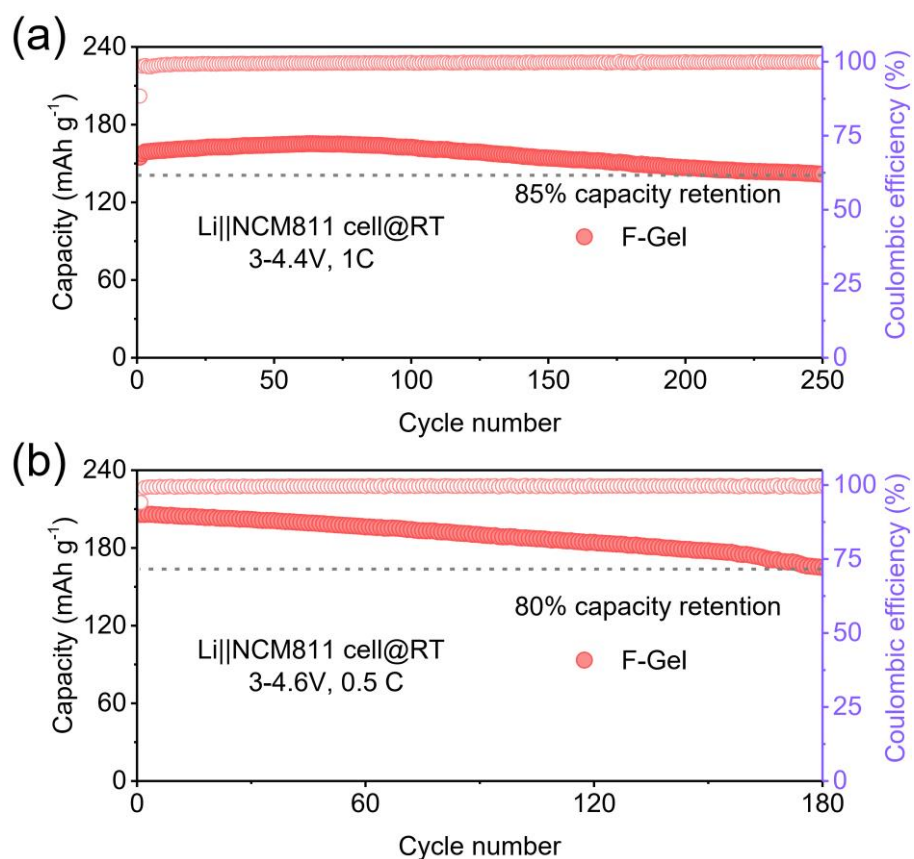
Fig. S34 The long-term cycling performance of Li|F-Gel|NCM811 battery with (a) a high cutoff voltage 4.4 V and (b) an ultrahigh cutoff voltage 4.6 V.

As shown in Supplementary Figure 34, the Li|F-Gel|NCM811 (1.5 mAh cm^{-2}) cells display high capacities retention of 85% and 80% over 400 and 180 cycles with 4.4 and 4.6 V cutoff-voltage at RT, respectively.
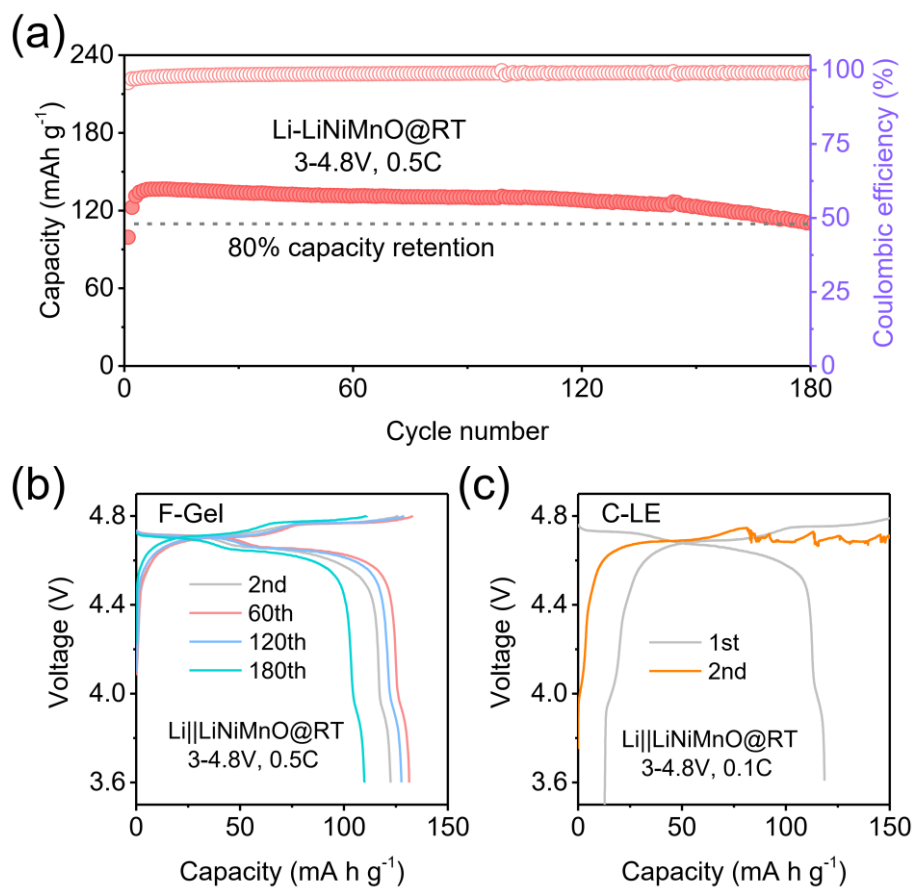
Fig. S35 (a) The long-term cycling performance of Li||LiNi$_{0.5}$Mn$_{1.5}$O$_4$ batteries with F-Gel electrolyte at RT. Charge–discharge voltage profiles of the Li||LiNi$_{0.5}$Mn$_{1.5}$O$_4$ cells with (b) F-Gel electrolyte and (c) C-LE at RT.

Another high-energy density cathode system LiNi$_{0.5}$Mn$_{1.5}$O$_4$ is also used to further demonstrate the high-voltage stability of F-Gel electrolyte. Coupled with F-Gel electrolyte, the Li||LiNi$_{0.5}$Mn$_{1.5}$O$_4$ cell delivered a capacity retention of 80% over 180 cycles in the voltage range of 3.6–4.8 V at 0.5 C under RT. By contrast, an obvious over-charge was observed at the 2nd charging cycle for Li|C-LE|LiNi$_{0.5}$Mn$_{1.5}$O$_4$ cell due to the lower oxidation stability of C-LE (4.2 V).
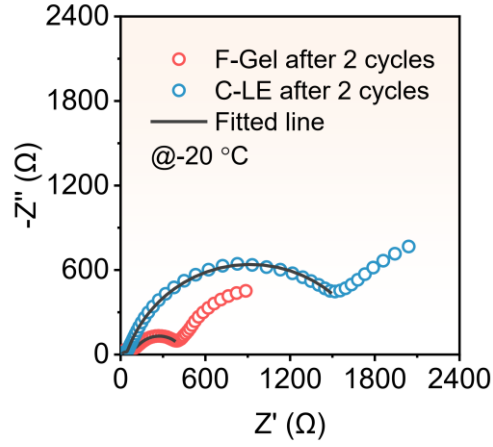
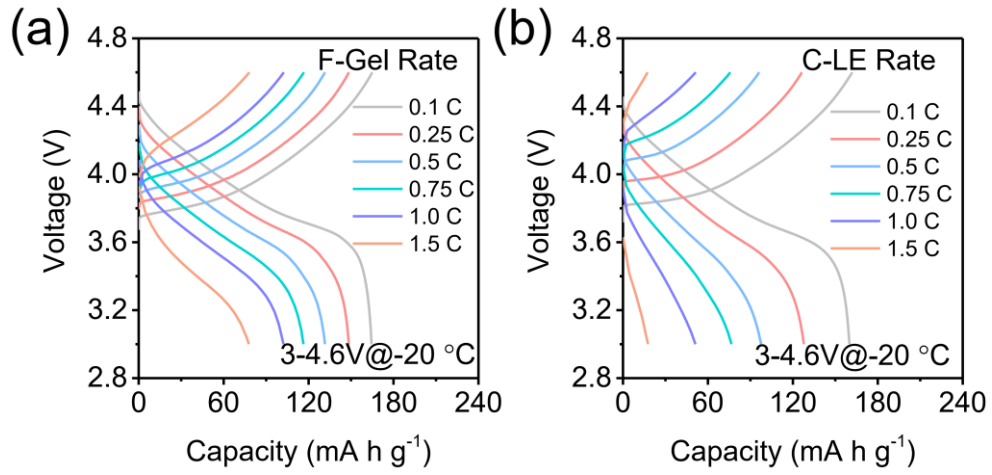**Fig. S36** The EIS curves of Li||NCM622 cells after activation for 2 cycles at 0.1 C under –20 ℃.

Fig. S37 Charge–discharge voltage profiles of the Li||NCM622 coin cells with different current densities at –20 ℃.

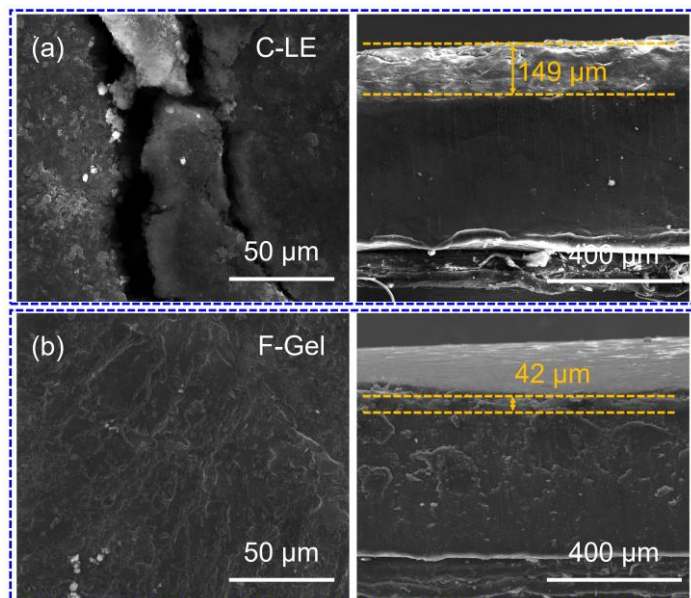**Fig. S38** SEM images illustrating morphologies of the lithium anode cycled in Li‖NCM622 coin cells with different electrolytes at –20 °C: (a) surface morphologies and cross-section views using C-LE electrolyte, and (b) surface morphologies and cross-section views using F-Gel.

The surface of cycled lithium anode retrieved from symmetric cell with F-Gel electrolyte is flatter and more compact with a SEI layer of 42 μm. As a comparison, the SEI thickness of C-LE is 149 μm due to the irreversible reaction between carbonyl group and lithium anode.
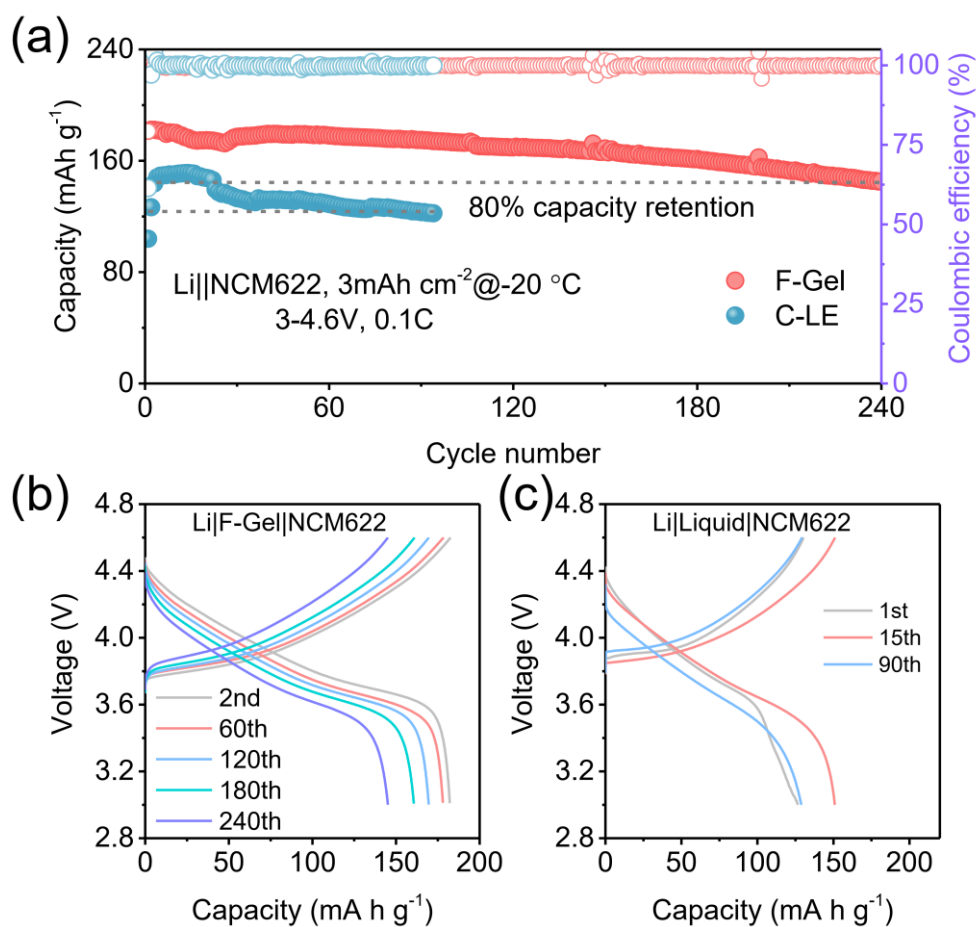
Fig. S39 (a) The long-term cycling performance of Li‖NCM622 batteries with both electrolyte under a high areal loading of 3 mAh cm^{-2} at –20 °C. The corresponding charge–discharge voltage profiles of the Li‖NCM622 coin cells at 2nd, 60th, 120th, 180th, and 240th cycles with (b) F-Gel electrolyte and (c) C-LE.
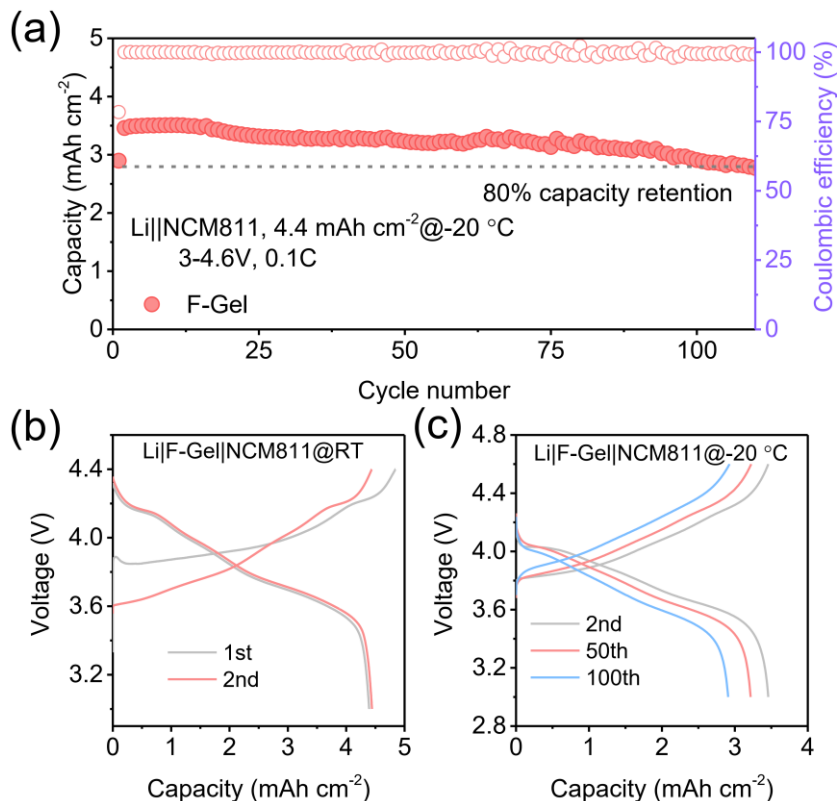
Fig. S40 (a) The long-term cycling performance of Li‖NCM811 batteries with both electrolyte under a high areal loading of 4.4 mAh cm^{-2} at –20 °C. (b) The 1st and 2nd charge–discharge voltage profiles of the Li‖NCM811 coin cell at RT with a 4.4 V cut-off voltage. (c) The corresponding charge–discharge voltage profiles of the Li‖NCM811 coin cell at –20 °C.
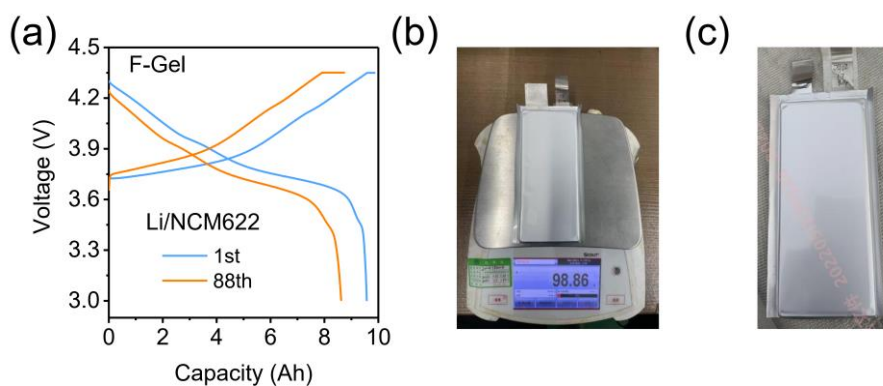

Fig. S41 (a) The 1st and 85th charge–discharge voltage profiles of 10 Ah Li|F-Gel|NCM622 pouch cell at RT with a 4.35 V cut-off voltage. (b) Optical image for the mass of the pouch cell. (c) Optical image of the pouch cell after cycling.
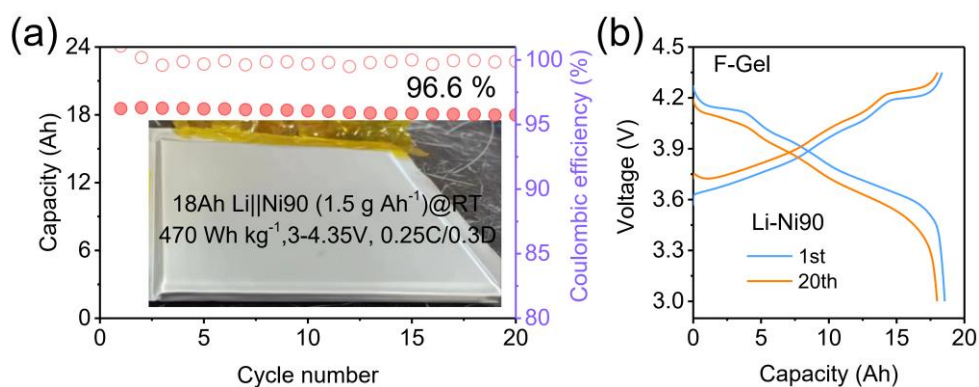
Fig. S42 (a) The long-term cycling performance of Li|F-Gel|LiNi$_{0.9}$Co$_{0.5}$Mn$_{0.5}$ (Ni90) batteries at RT at 0.25 C. The inset is optical image of the pouch cell before cycling. (b) The 1st and 20th charge–discharge voltage profiles of pouch cell.
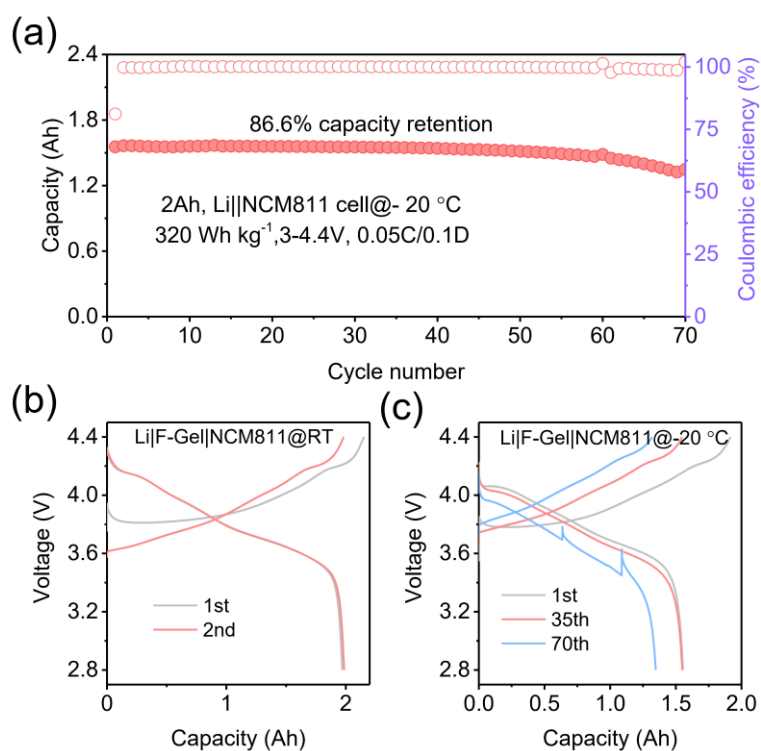

Fig. S43 (a) The long-term cycling performance of 2 Ah Li|F-Gel|NCM811 pouch cell at –20 °C. (b) The 1st and 2nd charge–discharge voltage profiles of the Li||NCM811 pouch cell at RT with a 4.4 V cut-off voltage. (c) The corresponding charge–discharge voltage profiles of the Li||NCM811 pouch cell at –20 °C.
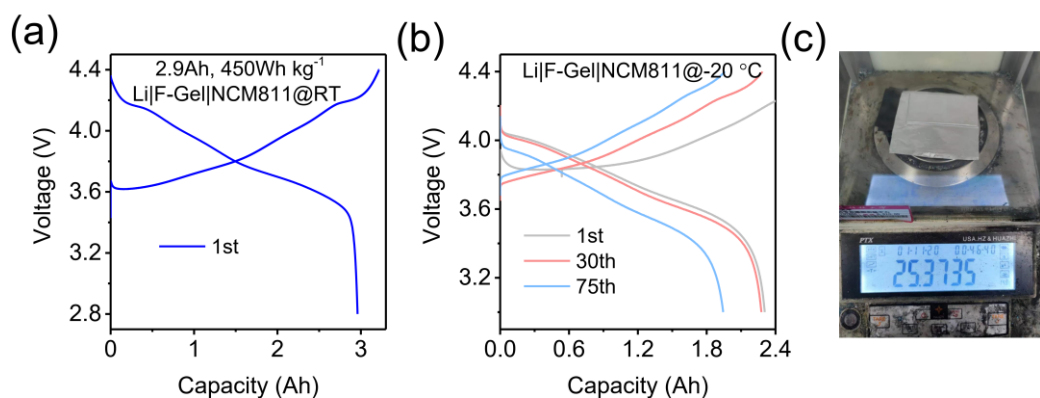
Fig. S44 (a) The 1st charge–discharge voltage profiles of the Li‖NCM811 pouch cell at RT with a 4.4 V cut-off voltage. (b) The corresponding charge–discharge voltage profiles of the 2.9 Ah Li‖NCM811 pouch cell at –20 ℃. (c) Optical image for the mass of the pouch cell.

|	Parameter	Value
	Specific capacity	205 mAh g^{-1}
NCM811 cathode	Areal weight (each side)	24.5 mg cm^{-2}
	Areal capacity (each side)	5 mAh cm^{-2}
	Number of layers	13
Al foil	Thickness	12 µm
	Specific capacity	3860 mAh g^{-1}
Li anode	Thickness	100 µm
	Number of layers	14
Cu foil	Thickness	0
Separator	Thickness	9 µm
Electrolyte	E/C ratio	1.55 g Ah^{-1}
Package foil	Thickness	88 µm
Pouch cell (3-4.4 V)	Total weight	25.37 g
	Capacity	2.9 Ah
Energy	@RT	11.4 Wh
	@–20 ℃	8.8 Wh
Energy density	@RT	450 Wh kg^{-1}
	@–20 ℃	350 Wh kg^{-1}

Fig. S45 Detailed parameters of the 2.9 Ah Li‖NCM811 pouch cell.
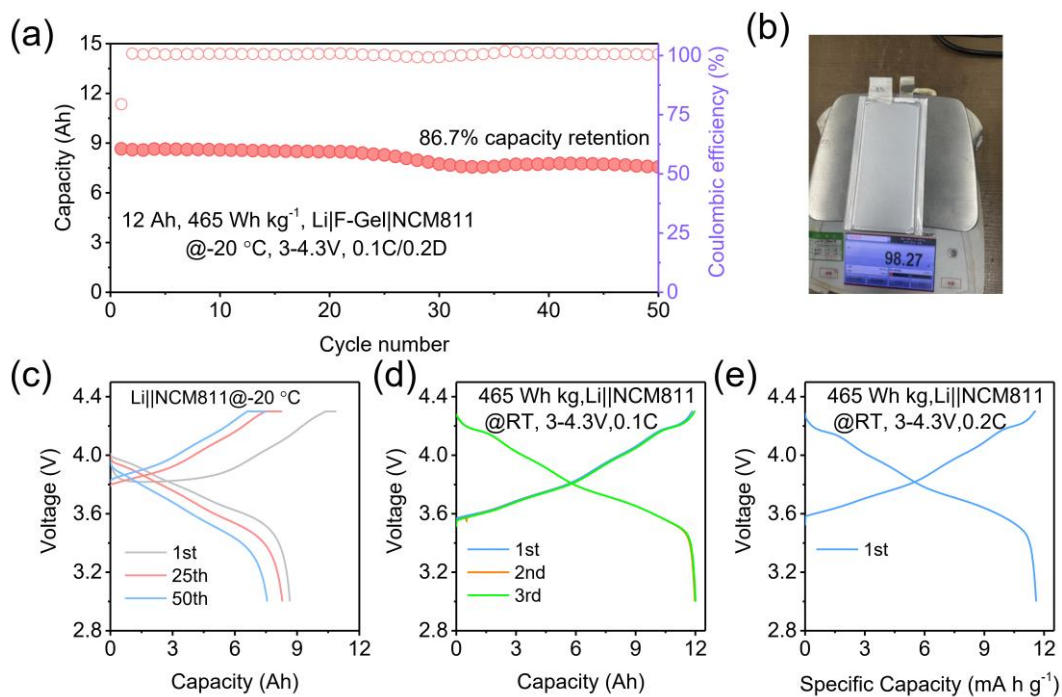
Fig. S46 (a) The long-term cycling performance of 12 Ah Li|F-Gel|NCM811 pouch cell at –20 °C. (b) Optical image for the mass of the 12Ah pouch cell. (c) The corresponding 1st, 25th and 50th charge–discharge voltage profiles of the Li||NCM811 pouch cell at –20 °C with a 4.3 V cut-off voltage. (d-e) The charge–discharge voltage profiles of the Li||NCM811 pouch cell at RT.
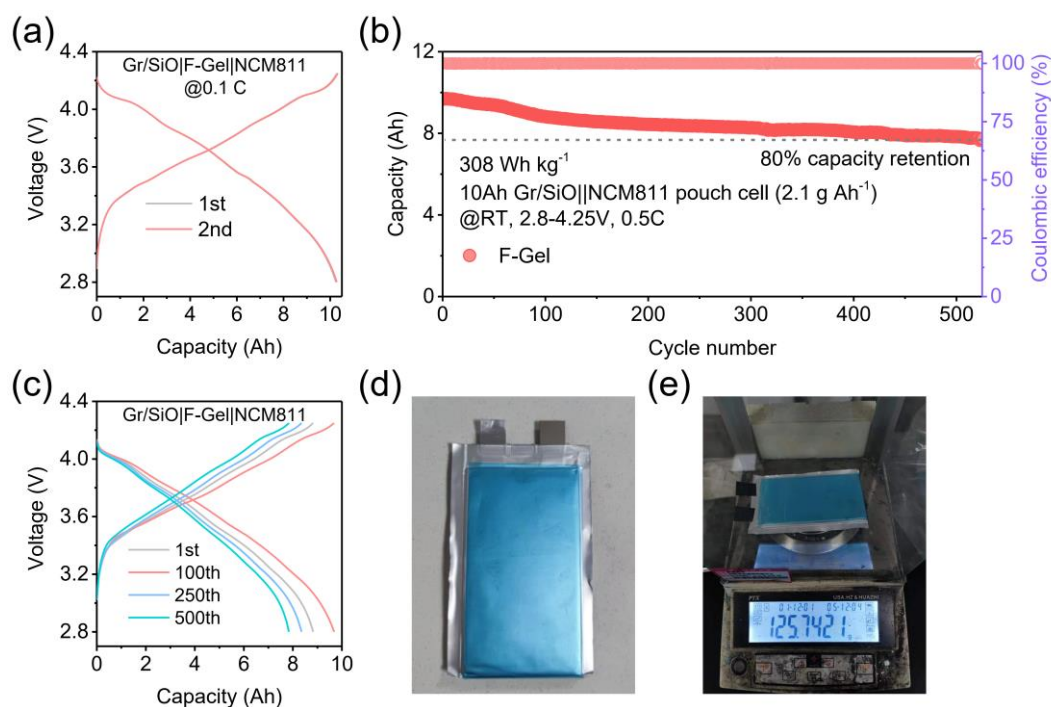
Fig. S47 (a) The 1st and 2nd charge–discharge voltage profiles of the Li‖NCM811 coin cells with a 4.25 V cut-off voltage at RT. (b) The long-term cycling performance of 10 Ah Gr/SiO|F-Gel|NCM811 pouch cell at RT. (c) The corresponding charge–discharge voltage profiles of the Gr/SiO‖NCM811 pouch cell with a 0.5 C rate at RT. (d) Digital photograph of the pouch cell before cycling. (e) Optical image for the mass of the pouch cell.

The feasibility of F-Gel electrolyte was also demonstrated by 10 Ah Gr/SiO‖NCM811 pouch cell at RT. The pouch cell displayed a high capacity retention of 80% with a low E/C ratio of 2.1 g Ah^{-1} over 550 cycles in the voltage range of 2.8–4.25 V at 0.5 C at RT. Based on the mass of the pouch cell and energy, the energy density was calculated to be 308 Wh kg^{-1}.
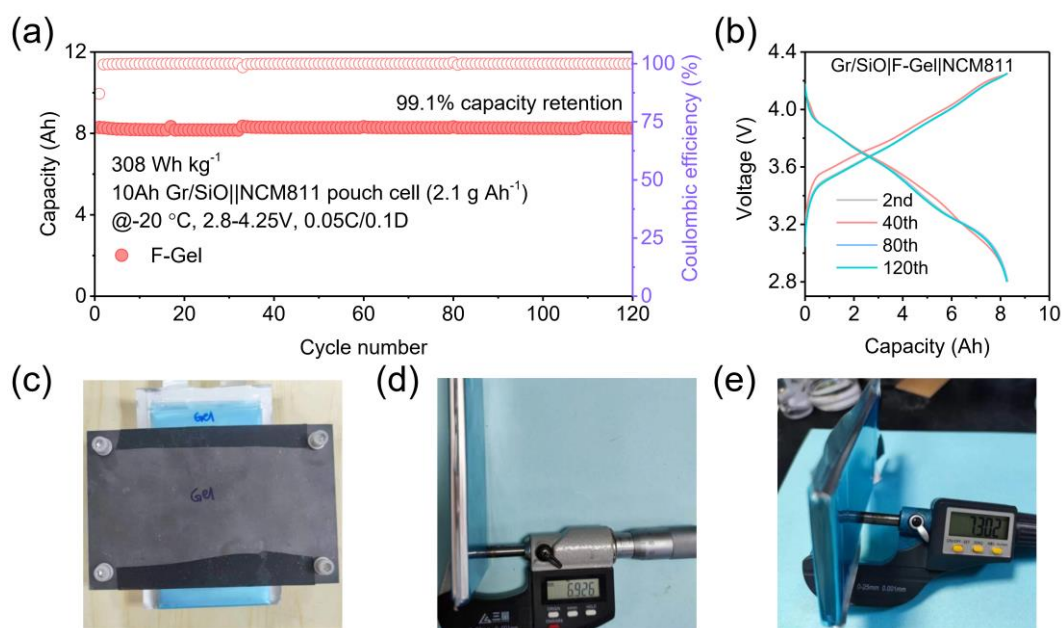
Fig. S48 (a) The long-term cycling performance of 10 Ah Gr/SiO|F-Gel|NCM811 pouch cell at –20 ℃. (b) The corresponding charge–discharge voltage profiles of the Gr/SiO||NCM811 cells. (c) The pressure jig for testing pouch cell. (d-e) Optical image for the thickness of the pouch cell: (d) before cycling, (e) after cycling.

At a low operation temperature of –20 ℃, the 10 Ah Gr/SiO||NCM811 pouch cell with F-Gel electrolyte shows high retention of their room-temperature capacity (8.29 Ah, 82.9%). After 100 cycles at –20 ℃, the pouch cell shows negligible capacity degradation (capacity retention 99.1%), which is comparable with the state-of-the-art performance of high-energy-density lithium-ion batteries. Besides, the thickness of pouch cell after 0 (6.926 mm) and 120 cycles (7.302 mm) was recorded. Thus, the cell swelling rate is 5.4% at the 120th cycle.

	Parameter	Value
NCM811 cathode	Specific capacity	200 mAh g^{-1}
	Areal weight (each side)	13 mg cm^{-2}
	Areal capacity (each side)	2.5 mAh cm^{-2}
	Number of layers	20
Al foil	Thickness	12 μm
Gr/SiO anode (80 wt%+14 wt%)	Specific capacity	513 mAh g^{-1}
	Areal capacity	2.65 mAh cm^{-2}
	Number of layers	21
	N/P ratio	1.06
Cu foil	Thickness	6 μm
Separator	Thickness	11 μm
Electrolyte	E/C ratio	2.1 g Ah^{-1}
Package foil	Thickness	88 μm
Pouch cell (2.8-4.25 V)	Total weight	125.7 g
	Capacity	10 Ah
Energy	@RT	38.7 Wh
	@−20 °C	29.1 Wh
Energy density	@RT	308 Wh kg^{-1}
	@−20 °C	231 Wh kg^{-1}

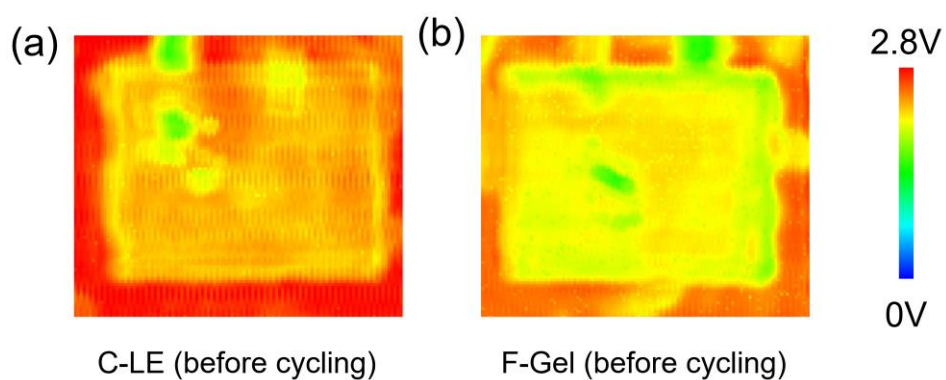**Fig. S49** Detailed parameters of the 10 Ah Gr/SiO||NCM811 pouch cell.

Fig. S50 Ultrasonic transmission mappings of Li||NCM622 pouch cell with (a) C-LE and (b) F-Gel electrolyte before cycling.
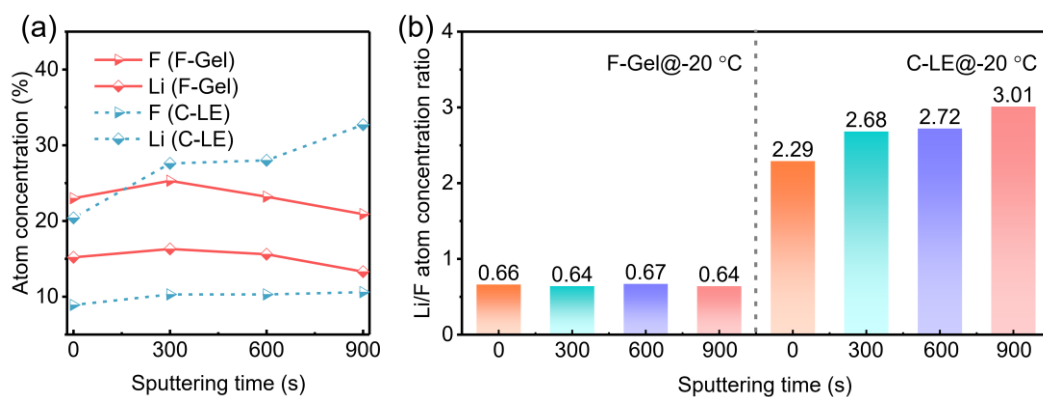
Fig. S51 (a) Elemental portions by XPS of cycled NCM622 in both electrolyte at –20 °C. (b) The corresponding Li/F atom concentration ratios in different electrolytes.
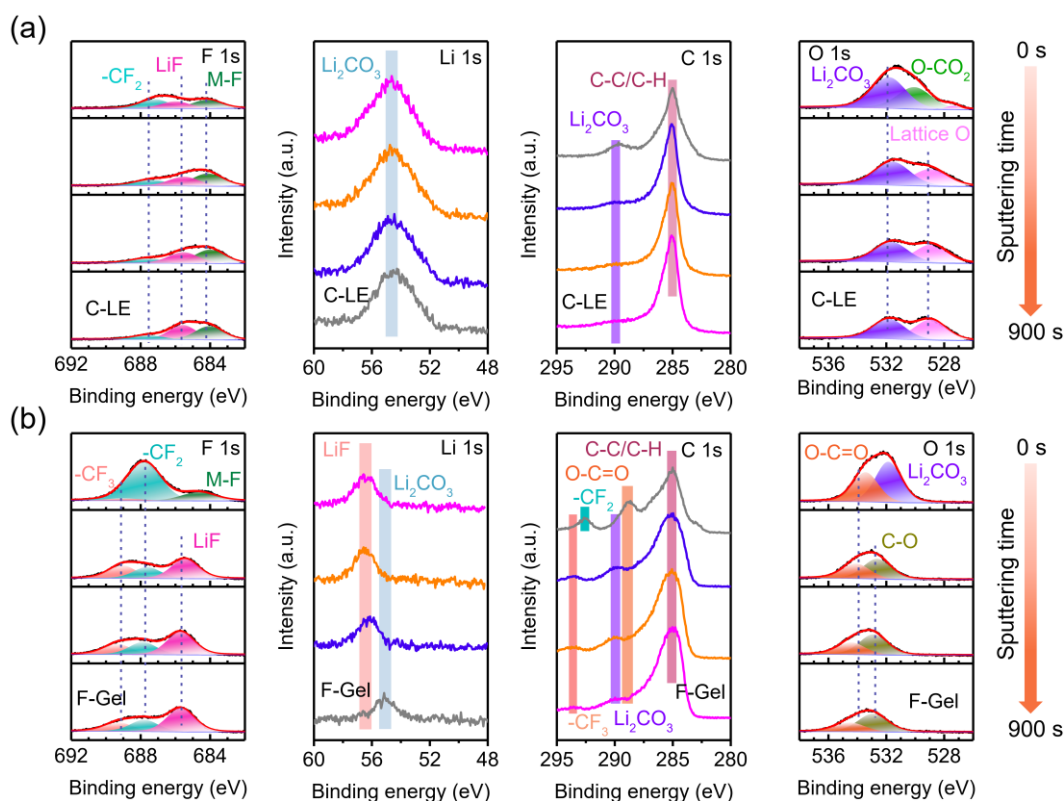

Fig. S52 (a-b) XPS depth profiles of F 1s, Li 1s, C 1s and O1s spectra obtained from the cycled NCM622 cathode collected from (a) Li|C-LE|NCM622 and (b) Li|F-Gel|NCM622 cells at RT.

Compared with the cathode cycled in the reference C-LE, the one cycled in the F-Gel electrolyte has a much stronger LiF peak and weaker M–F peak accompanied by the $-CF_3$ peak. In addition, the F-Gel electrolyte shows much weaker Li 1s and C 1s signal, indicating the suppress CEI growth and TMs dissolution.
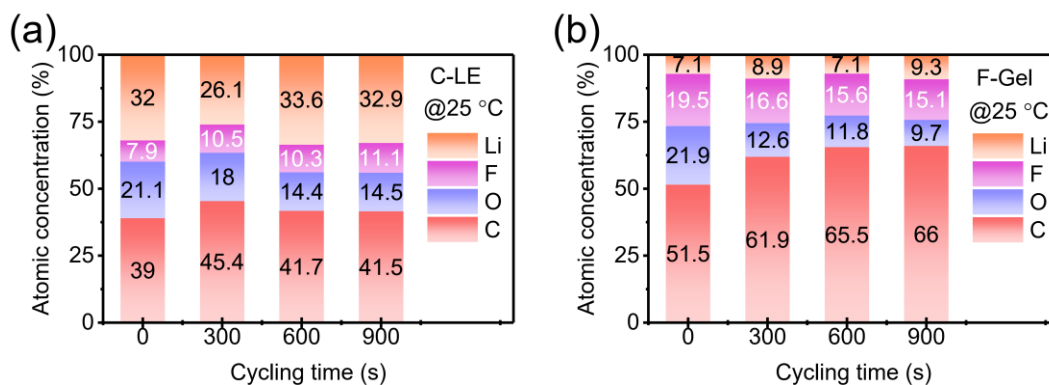
Fig. S53 Elemental portions by XPS of NCM622 cathode at RT in (a) C-LE and (b) F-Gel electrolyte.

It is found that F and C elements account for larger portions in the F-Gel electrolyte compared with that of C-LE at RT. Besides, the CEI formed in F-Gel electrolyte shows a lower content of Li element than that of C-LE, indicating the suppressed lithium salt decomposition under high-voltage operation.
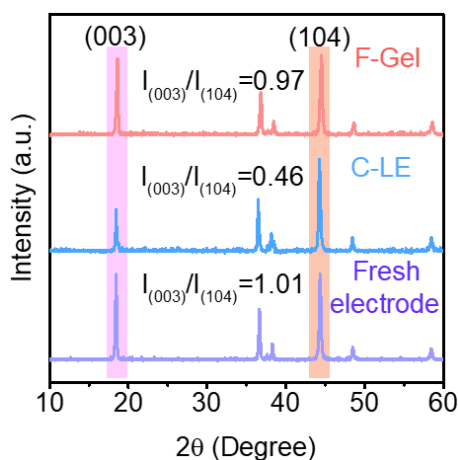

Fig. S54 XRD patterns of fresh NCM622 electrode and the cycled NCM622 electrode in both electrolytes at –20 °C.
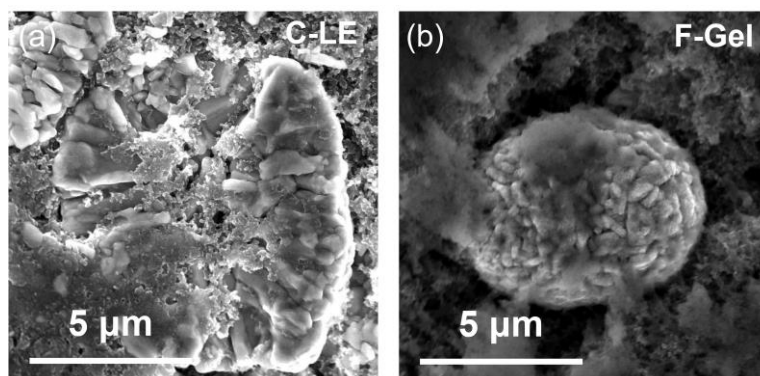
Fig. S55 SEM images of NCM622 electrodes after 50 cycles using (a) C-LE and (b) F-Gel electrolyte with a 4.6 V cut-off voltage at –20 °C.

Table S1. Physical and chemical properties of electrolyte solvents used in this study.

Solvent	Melting point (ºC)	Boling point (ºC)	Density (g cm^{-3})	Viscosity (cP)	Solubility of LiPF$_6$ (mol L^{-1})	LUMO (eV)	HOMO (eV)
EA	–83.9	77.0	0.90	0.407	3.3	–1.09	–6.03
F-EA	–65.5	119.3	1.10	0.818	2.8	–1.29	–6.51
2F-EA	–80.0	99	1.18	0.662	2	–2.24	–6.77
3F-EA	–62.0	61	1.19	0.384	< 0.5	–2.31	–7.06
EA-2F	–80.0	105	1.17	0.953	3	–1.41	–6.57
EA-3F	–85.17	78	1.26	0.605	2.7	–1.33	-5.97

Table S2. EIS fitting results of Li‖Li cells with both electrolytes at –20 °C.

Electrolyte	$R_{electrolyte}$ (Ω)	$R_{SEI+CEI}$ (Ω)	$T_{SEI+CEI}$ (10^{-6} F)	$R_{de\text{-}solvation}$ (Ω)	$T_{de\text{-}solvation}$ (10^{-5} F)
F-Gel	9.27	47.6	4.89	368.9	7.06
C-LE	11.3	38.5	2.89	1750	5.26

References

1. B. D. Adams, J. Zheng, X. Ren, W. Xu and J.-G. Zhang, *Adv. Energy Mater.*, 2018, **8**, 1702097.
2. Y. Zhao, T. Zhou, T. Ashirov, M. El Kazzi, C. Cancellieri, L. P. H. Jeurgens, J. W. Choi and A. Coskun, *Nat. Commun.*, 2022, **13**, 2575.
3. S. Plimpton, *J. Comput. Phys.*, 1995, **117**, 1-19.
4. N. Kumar and J. M. Semi nario, *J. Phys. Chem. C*, 2016, **120**, 16322-16332.
5. M. Takeuchi, Y. Kameda, Y. Umebayashi, S. Ogawa, T. Sonoda, S.-i. Ishiguro, M. Fujita and M. Sano, *J. Mol. Liq.*, 2009, **148**, 99-108.
6. B. Doherty, X. Zhong, S. Gathiaka, B. Li and O. Acevedo, *J. Chem. Theory Comput.*, 2017, **13**, 6131-6145.
7. T. Lu and F. Chen, *J. Comput. Chem.*, 2012, **33**, 580-592.
8. J. Zhang and T. Lu, *Phys. Chem. Chem. Phys.*, 2021, **23**, 20323-20328.
9. Z. Yu, H. Wang, X. Kong, W. Huang, Y. Tsao, D. G. Mackanic, K. Wang, X. Wang, W. Huang, S. Choudhury, Y. Zheng, C. V. Amanchukwu, S. T. Hung, Y. Ma, E. G. Lomeli, J. Qin, Y. Cui and Z. Bao, *Nat. Energy*, 2020, **5**, 526-533.
10. Z. Yu, P. E. Rudnicki, Z. Zhang, Z. Huang, H. Celik, S. T. Oyakhire, Y. Chen, X. Kong, S. C. Kim, X. Xiao, H. Wang, Y. Zheng, G. A. Kamat, M. S. Kim, S. F. Bent, J. Qin, Y. Cui and Z. Bao, *Nat. Energy*, 2022, **7**, 94-106.
11. M. Jia, P. Wen, Z. Wang, Y. Zhao, Y. Liu, J. Lin, M. Chen and X. Lin, *Adv. Functional Mater.*, 2021, **31**, 2101736.
12. S.-J. Yang, N. Yao, F.-N. Jiang, J. Xie, S.-Y. Sun, X. Chen, H. Yuan, X.-B. Cheng, J.-Q. Huang and Q. Zhang, *Angew. Chem., Int. Ed.*, 2022, **61**, e202214.
13. X. Fan, X. Ji, L. Chen, J. Chen, T. Deng, F. Han, J. Yue, N. Piao, R. Wang, X. Zhou, X. Xiao, L. Chen and C. Wang, *Nat. Energy*, 2019, **4**, 882-890.